Chemical Science

EDGE ARTICLE

View Article Online
View Journal

Cite this: DOI: 10.1039/d6sc01958g

All publication charges for this article have been paid for by the Royal Society of Chemistry

De novo design of NIR-II thioxanthene dye and phosphate-driven charge transfer-coupled *J*-aggregates for high resolution tumor angiography and type I phototherapy against hypoxic tumors

Chuangli Zhang, Ziyong Wu, Yang Bai, Jing He, Mengyuan Miao, Feiyu Diao, Qingzhi Wang, Shan Zhong, Pengfei Shi,* Xin-Yue Song* and Shusheng Zhang*

Received 10th March 2026
Accepted 12th June 2026

DOI: 10.1039/d6sc01958g

rsc.li/chemical-science

Regulating the photophysical properties of NIR-II dyes *via* atomic engineering to inhibit type II reactive oxygen species (ROS, $^1O_2$) generation and only generate type I ROS ($O_2^{\bullet-}$ and $^{\bullet}OH$), and modulating dye aggregation for fabricating charge transfer (CT)-coupled *J*-aggregates (J_{CT}-aggregates) to amplify $O_2^{\bullet-}$ and $^{\bullet}OH$ yield remain major challenges with rare reports. Herein, we *de novo* designed a NIR-II thioxanthene dye SOH. The heavy atom effect of sulfur and the twisted conjugated skeleton strengthened spin–orbit coupling (SOC) by 9.3-fold and intersystem crossing (ISC) efficiency by 86.5-fold and reduced the lowest triplet excited state (T_1) energy level to 0.959 eV, completely inhibiting $^1O_2$ generation while only initiating $O_2^{\bullet-}$ and $^{\bullet}OH$ production, with a photothermal conversion efficiency (PCE) of 42.3%. Furthermore, electrostatic interactions between phosphates (HPO_4^{2-}) and the positively charged skeleton of SOH drove the formation of J_{CT}-aggregates (P-SOH NPs), leading to a prominent redshift (beyond 350 nm) of absorption/emission to 1120/1134 nm, 36.1-fold fluorescence enhancement, 59.0-fold increased type I ROS yield, and PCE elevated to 51.1%. P-SOH NPs achieved NIR-II high-resolution tumor angiography (fluorescence resolution: 0.34 mm, signal-to-background ratio (SBR) = 4.56; photoacoustic resolution: 0.11 mm, SBR = 17.2). The type I phototherapy of P-SOH NPs maintained high tumor cell killing efficiency even in hypoxia, achieving complete tumor ablation.

Introduction

The hypoxic characteristics of the solid tumor microenvironment were a core bottleneck that limited the efficacy of conventional type II photodynamic therapy (type II PDT). Over 90% of advanced solid tumors contained hypoxic regions with a local oxygen partial pressure below 2%, which directly impaired the therapeutic efficiency of type II PDT.[1–3] The core mechanism of type II PDT was that photosensitizers, after excitation by laser irradiation, underwent intersystem crossing (ISC) to reach the triplet excited state, and then transferred energy to molecular oxygen to generate singlet oxygen ($^1O_2$). However, the scarcity of molecular oxygen in hypoxic environments led to a sharp decline in $^1O_2$ production, ultimately resulting in therapeutic failure.[4–6] Although researchers attempted to supplement local oxygen in tumors through strategies such as oxygen carrier delivery and *in situ* hydrogen peroxide decomposition, these approaches generally suffered from complex operations, limited oxygen diffusion range, and potential biosafety risks, making it difficult to fundamentally overcome the hypoxia-induced limitations.[7–9] In sharp contrast, type I PDT and photothermal therapy (PTT) provided novel solutions for hypoxic tumor treatment by virtue of their oxygen-independent properties. Type I PDT generated superoxide anion radicals ($O_2^{\bullet-}$) and hydroxyl radicals ($^{\bullet}OH$) through electron transfer or hydrogen abstraction between excited-state photosensitizers and substrates. The production of these ROS did not directly rely on molecular oxygen, enabling the maintenance of high-efficiency tumor-killing effects even in severely hypoxic environments.[10–13] PTT was completely oxygen-independent and it converted light energy into thermal energy *via* photosensitizers to elevate the local temperature of tumors and achieve thermal ablation.[14–16] More importantly, compared with the first near-infrared (NIR-I) region, excitation light in the second near-infrared window (NIR-II, 1000–1700 nm) exhibited stronger tissue penetration depth (up to 5–20 mm) and lower photodamage to biological tissues. Its higher maximum permissible

---

Shandong Provincial Key Laboratory of Tumor Imaging Equipment Development and Diagnosis & Treatment Integration Technology, School of Chemistry and Chemical Engineering, College of Medicine, Linyi University, Linyi 276000, P. R. China. E-mail: shipengfei913@163.com; songxinyue428@163.com; shushzhang@126.com

exposure (MPE) dose could enhance the therapeutic depth while reducing the risk of normal tissue injury.[17–20] Therefore, the development of dyes with integrated NIR-II absorption, efficient type I ROS generation ($O_2^{\bullet -}$ and $^{\bullet}OH$), and high PCE had emerged as a core research direction for efficient phototherapy of hypoxic tumors.

Currently, the rational design of molecular structures of NIR-II dye and precise regulation of directional type I ROS generation are mainstream strategies. The core principle was to reduce the triplet energy level (E_T < 0.98 eV) through molecular configuration design and electronic structure modulation, block the energy transfer to ground-state oxygen for $^1O_2$ generation, and prioritize the initiation of electron transfer pathways to directionally produce $O_2^{\bullet -}$ and $^{\bullet}OH$.[21,22] For instance, the introduction of strong electron-donating/withdrawing groups (triphenylamine (TPA)/BODIPY;[21] TPA/rhodanine;[23] TPA/-CF_3;[24] TPA/PPQ;[25] julolidine/BODIPY and pyridine;[26] Y6/Th;[27] COi6/Cl[28]) or the optimization of conjugated π-bridges (benzene[29] and thiophene[24,30]) into dye molecules could enhance the intramolecular charge transfer (ICT) effect, narrow the singlet-triplet energy gap (ΔE_{ST}), and improve ISC efficiency. The utilization of twisted molecular skeletons could disrupt intermolecular π–π stacking, promote spin–orbit charge-transfer intersystem crossing (SOCT-ISC), avoid aggregation-caused quenching (ACQ), and simultaneously enhance electron transfer for type I ROS production.[23,31] The application of acceptor-triggered photoinduced electron transfer (a-PET) could facilitate the separation of electron–hole pairs, thereby boosting type I ROS generation.[32] The construction of open-shell diradical configurations *via* large π-conjugated systems to stabilize unpaired electrons could reduce ΔE_{ST} and promote photoinduced charge separation.[33] The employment of the heavy atom effect (*e.g.*, tellurium (Te)) could enhance spin–orbit coupling (SOC) to directionally generate $O_2^{\bullet -}$.[34] In addition, the aggregate engineering of NIR-II dyes to reinforce the synergy between electron transfer and photothermal conversion was also an effective design strategy. For example, optimizing molecular structures to enable dyes to assemble into charge-transfer (CT)-coupled *J*-aggregates *via* intermolecular electrostatic attraction with short-range orbital overlap, intermolecular distances <4 Å, and distinct orbital overlap, boosted the yield of type I ROS and promoted nonradiative decay for improved PCE.[35–38] Compared with the traditional *J*-aggregates driven by hydrophobic interactions, intermolecular π–π stacking, or hydrogen bonds, J_{CT}-aggregates realized a spectral redshift of more than 200 nm, directly advancing the absorption/emission of the dye from the NIR-I window to the NIR-II window, and avoiding the ACQ defect.[39–41] Nevertheless, the aforementioned strategies were commonly plagued by cumbersome organic synthesis and failed to concurrently integrate a large spectral red-shift (>350 nm), efficient NIR-II absorption (>1100 nm), a high yield of type I ROS, superior PCE (>50%), and NIR-II dual-modal fluorescence (FL) and photoacoustic (PA) tumor angiography.

In this contribution, we designed and developed a novel NIR-II thioxanthene dye, SOH (Scheme 1), from scratch. By precisely introducing a sulfur atom into the molecular skeleton and regulating the molecular aggregates with phosphates, we achieved high-resolution NIR-II FL/PA bimodal tumor angiography and efficient synergy between type I PDT and PTT. At the molecular design level, the core innovations of SOH lay in the precise introduction of sulfur atoms and the optimization of the conjugated system. First, the strong electron-donating ability of

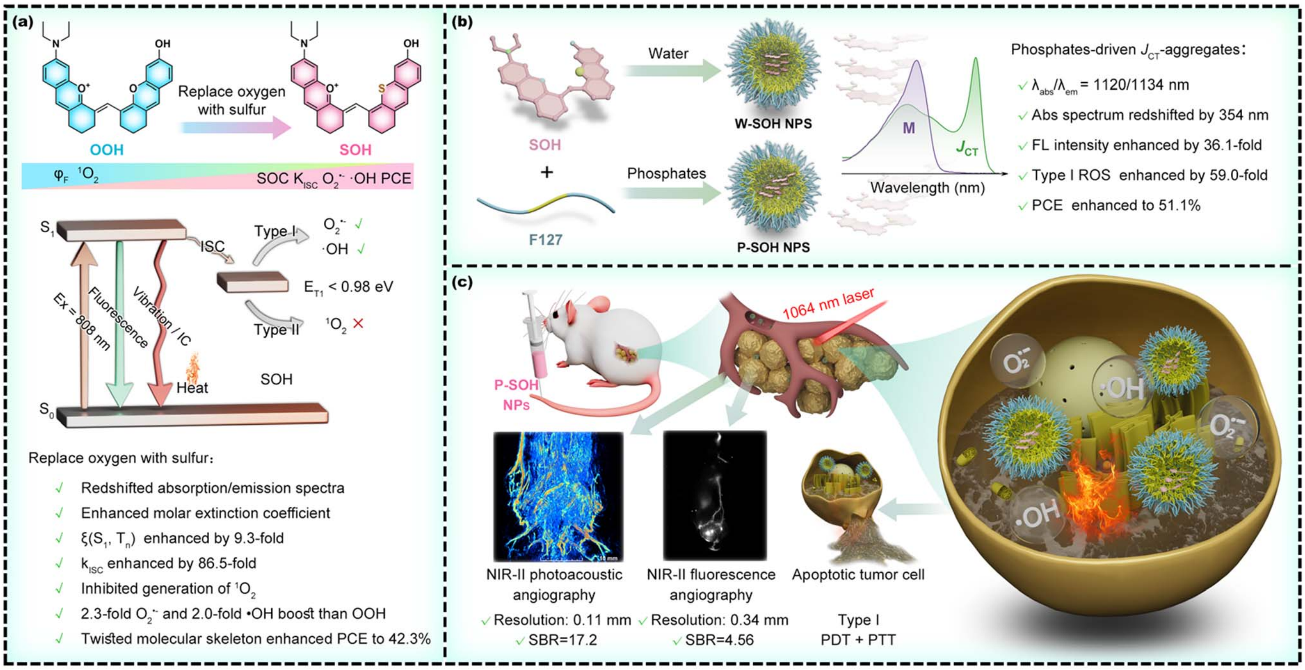

Scheme 1 Schematic illustrations of (a) design of NIR-II thioxanthene dye SOH and (b) phosphate-driven charge transfer-coupled *J*-aggregates (J_{CT}-aggregates) for (c) high resolution tumor angiography and type I PDT and PTT against hypoxic tumors.

sulfur atoms promoted the ICT effect, which redshifted the absorption wavelength of SOH to 679–888 nm and extended the emission wavelength to 919–983 nm. The molar extinction coefficient of SOH reached 53 570 M^{-1} cm^{-1}, significantly enhancing the NIR-II light absorption efficiency. Second, substituting the oxygen atom in the NIR-II xanthene dye OOH with a sulfur atom, the heavy atom effect of sulfur and more twisted molecular backbone significantly strengthened the SOC effect (enhanced by 9.3-fold), increasing the ISC efficiency by 86.5-fold. Meanwhile, this reduced the lowest triplet excited state (T_1) energy level of the dye to 0.959 eV (lower than the oxygen triplet–singlet transition energy of 0.98 eV), thus completely inhibiting the generation of type II ROS and enabling the exclusive production of type I ROS, which was suitable for hypoxic tumor treatment. Third, the sulfur atom-induced distortion of the molecular skeleton enhanced non-radiative transition, resulting in a PCE of 42.3% for SOH, which was much higher than that of the oxygen-substituted control dye OOH (26.1%), realizing the synergistic enhancement of type I PDT and PTT. At the aggregate regulation level, SOH innovatively formed phosphate-driven CT-coupled *J*-aggregates (P-SOH NPs) through electrostatic interactions between the positively charged regions on the molecular surface and HPO_4^{2-}. This assembly further redshifted the absorption/emission peaks to 1120/1134 nm, increased the fluorescence intensity by 36.1-fold, improved the type I ROS generation efficiency by 59.0-fold, and elevated the PCE to 51.1%. NIR-II fluorescence angiography of P-SOH NPs achieved a signal-to-background ratio (SBR) of 4.56, enabling clear identification of tumor microvessels (resolution: 0.34 mm). NIR-II photoacoustic angiography exhibited a high SBR of 17.2, which could accurately delineate the tumor vascular network (resolution: 0.11 mm). The synergistic effect of type I ROS and PTT led to a tumor cell apoptosis rate exceeding 95%, and this high-efficiency killing effect was maintained even in hypoxic environments. This study provided a new paradigm for the design and aggregate regulation of NIR-II type I dyes, realizing high-resolution tumor angiography and efficient phototherapy of hypoxic tumors.

Results and discussion

De novo design of NIR-II thioxanthene dye SOH

Polymethine dyes have the advantages of simple synthesis, high molar extinction coefficients, tunable absorption/emission wavelengths, and good biocompatibility, and are a kind of dye molecular platform that can realize NIR-II excitation.[42–44] Indocyanine green (ICG) is a typical polymethine dye, also known as cyanine dye, that has been approved for clinical use.[45,46] However, ICG cannot achieve phototheranostics under NIR-II excitation due to its intrinsic drawbacks, including a short absorption and emission wavelength. In order to redshift the absorption/emission spectra of the polymethine dyes, researchers modified the ICG molecule. ICG is composed of indole heterocycles at both ends and a π-bridge conjugated with carbon–carbon double bonds in the middle. When a carbon–carbon double bond is added to the conjugated π bridge in the middle, the maximal absorption/emission wavelength of the dye is red-shifted by about 100 nm. However, an excessive increase in the number of carbon–carbon double bonds leads to serious free rotation in the dye molecule and poor chemical stability and photostability. Therefore, replacing the two ends of the indole heterocycle with other types of groups is an appropriate design strategy.[47–49] Xanthene dyes generally possess high fluorescence quantum yields due to the rigid molecular structure that restricts free intramolecular rotation. In previous work, we developed the NIR-I xanthene dye Me-hNR with ultra-high fluorescence quantum yield up to 92%,[50] and a series of NIR-II xanthene dyes (CL1–CL4,[14] CM1–CM2,[20] CN1–CN3,[51] LY,[52] and LD[53]) with maximal emission exceeding 1200 nm. Long-wavelength NIR-II xanthene dyes can be obtained by replacing the indole heterocycles at both ends of ICG with xanthene groups. However, the non-radiative decay rates of the excited state of these long-wavelength dyes are fast, the released heat dominates the energy dissipation, and reactive oxygen species are not generated. In fact, these NIR-II xanthene dyes possess three intramolecular carbon–carbon double bonds. As a compromise strategy, we reduce the number of carbon–carbon double bonds to one, and the obtained xanthene dye can emit NIR-II fluorescence, generate reactive oxygen species (type I and type II) and heat, and achieve an effective balanced utilization of the excited state energy.

Sulfur atoms have a strong electron donating ability. Introducing a sulfur atom into the dye holds promise for enhancing the molar extinction coefficient and promoting the intramolecular charge transfer, which leads to the reduction of the energy gap and the red shift of absorption and emission wavelengths, and inhibits the radiative decay of excited molecules, resulting in partial fluorescence quenching and enhanced ROS generation and PCE. With these thoughts in mind, we *de novo* design NIR-II thioxanthene dye SOH (Scheme 1) by a nucleophilic substitution reaction of *m*-hydroxy thiophenol with CL-1. To demonstrate the superiority of introducing a sulfur atom, we attempted to replace the sulfur atom in the dye with an oxygen atom, but unfortunately the same synthetic step could not be used to obtain the dye OOH (Scheme 1) due to the insufficient nucleophilicity of resorcinol. Therefore, the xanthene groups of the two parts were directly coupled through a Knoevenagel condensation reaction to obtain the dye OOH. The detailed synthesis routes of SOH and OOH are described in Scheme S1. SOH and OOH have been fully characterized by ^{1}H NMR and ^{13}C NMR and high-resolution mass spectrometry (HRMS), as shown in Fig. S44–S49.

Photophysical properties, reactive oxygen species generation, and photothermal performance of dye SOH

We systematically investigated the photophysical properties, ROS generation capabilities, and photothermal performance of dyes OOH and SOH. The photophysical properties of the two dyes showed significant solvent dependence (Fig. 1a–d, Tables 1 and 2, Fig. S1–S5). The maximum absorption wavelength (λ_{abs}) of OOH ranged from 654 to 857 nm, and its fluorescence emission wavelength (λ_{em}) was 855–935 nm. In contrast, both

λ_{abs} and λ_{em} of SOH were red-shifted compared to those of OOH, spanning 679–888 nm and 919–983 nm, respectively, which was favorable for biological tissue penetration. With the increase in solvent polarity from low-polarity $CHCl_3$ to high-polarity DMF and DMSO, the Stokes shift ($\Delta\lambda$) of both dyes increased significantly. The $\Delta\lambda$ of OOH increased from 15 nm (in $CHCl_3$) to 253 nm (in DMF), while that of SOH increased from 53 nm (in $CHCl_3$) to 281 nm (in DMF). This phenomenon was attributed to the enhanced dipole moment difference between the excited state and the ground state induced by increased solvent polarity, which was consistent with the twisted intramolecular charge transfer (TICT) mechanism.[54] OOH exhibited overall superior fluorescence quantum yield (Φ_F) and brightness ($\varepsilon \times \Phi_F$) compared to SOH. OOH achieved the best performance in $CHCl_3$ with Φ_F = 0.36% and brightness = 162 M^{-1} cm^{-1}, whereas the highest Φ_F of SOH was only 0.09% (in THF) and the maximum brightness was 43 M^{-1} cm^{-1} (in $CHCl_3$).[55] Notably, SOH showed a higher molar extinction coefficient (ε) than OOH in low-polarity solvents, with ε = 53 570 M^{-1} cm^{-1} in $CHCl_3$, indicating stronger light absorption capacity of SOH.

Under 808 nm laser irradiation, the two dyes differed in the type and yield of ROS generated, which was further confirmed by electron paramagnetic resonance (EPR) spectroscopy. From the degradation curve of DPBF (a $^1O_2$ probe) (Fig. 1e and S6), SOSG (Fig. S7) and EPR measurements (Fig. 1i), OOH could efficiently generate $^1O_2$, while SOH failed to produce $^1O_2$. Based on the fluorescence enhancement curves of DHE (a $O_2^{\bullet-}$ probe) (Fig. 1f and S8), HPF (a $^{\bullet}OH$ probe) (Fig. 1g and S9), DCFH (a total ROS probe) (Fig. 1h and S10), and EPR tests (Fig. 1j and k),

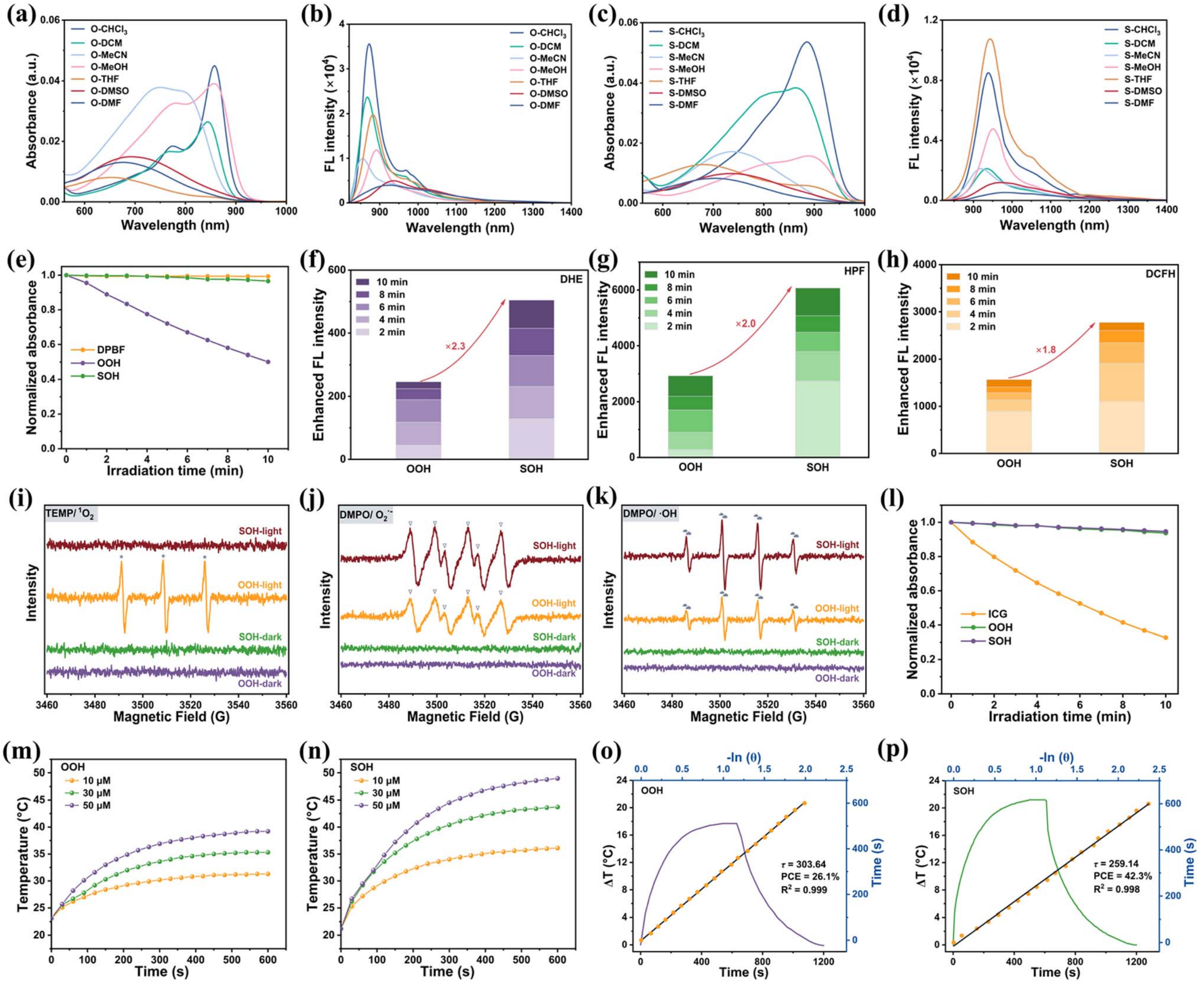

Fig. 1 (a) Absorption spectra of dye OOH in solvents of different polarities. (b) Fluorescence spectra of dye OOH in solvents of different polarities (excitation wavelength: 808 nm). (c) Absorption spectra of dye SOH in solvents of different polarities. (d) Fluorescence spectra of dye SOH in solvents of different polarities (excitation wavelength: 808 nm). The following tests were all performed under 808 nm laser irradiation. Evaluation of (e) $^1O_2$, (f) $O_2^{\bullet-}$, (g) $^{\bullet}OH$, and (h) total ROS generation capabilities of dyes OOH and SOH, respectively. Detection of (i) $^1O_2$, (j) $O_2^{\bullet-}$, and (k) $^{\bullet}OH$ generation capabilities of dyes OOH and SOH using an electron paramagnetic resonance (EPR) spectrometer, respectively. (l) Evaluation of the photostability of dyes OOH and SOH with ICG as a control. (m) Photothermal effect of dye OOH. (n) Photothermal effect of dye SOH. (o) Evaluation of the photothermal conversion efficiency of dye OOH. (p) Evaluation of the photothermal conversion efficiency of dye SOH.

Table 1 Photophysical properties of dye OOH

Solvents	λ_{abs}^{max} (nm)	λ_{em}^{max} (nm)	Stokes shift $\Delta\lambda$ (nm)	ε (M^{-1} cm^{-1})	$\Phi_F{}^a$ (%)	Brightness, $\varepsilon \times \Phi_F$ (M^{-1} cm^{-1})
$CHCl_3$	857	872	15	44 900	0.36	162
DCM	844	867	23	26 440	0.24	63
MeCN	750	855	105	37 880	0.10	38
MeOH	857	891	34	39 080	0.12	47
THF	654	882	228	8100	0.20	16
DMSO	692	935	243	14 940	0.05	7
DMF	677	930	253	13 080	0.04	5

[a] Dye IR-26 ($\Phi_F = 0.05\%$ in dichloroethane) was used as a reference.

Table 2 Photophysical properties of dye SOH

Solvents	λ_{abs}^{max} (nm)	λ_{em}^{max} (nm)	Stokes shift $\Delta\lambda$ (nm)	ε (M^{-1} cm^{-1})	$\Phi_F{}^a$ (%)	Brightness, $\varepsilon \times \Phi_F$ (M^{-1} cm^{-1})
$CHCl_3$	886	939	53	53 570	0.08	43
DCM	865	933	70	38 400	0.04	15
MeCN	739	919	180	17 170	0.04	7
MeOH	888	951	63	15 730	0.06	9
THF	679	943	264	12 870	0.09	12
DMSO	734	973	239	9860	0.03	3
DMF	702	983	281	8280	0.02	2

[a] Dye IR-26 ($\Phi_F = 0.05\%$ in dichloroethane) was used as a reference.

SOH exhibited significantly higher production capacity of $O_2{}^{\bullet-}$ (2.3-fold), $^{\bullet}$OH (2.0-fold), and total ROS (1.8-fold) compared to OOH. Thus, SOH exhibited superior photoinduced electron transfer efficiency, enabling efficient generation of type I ROS, which provided a core foundation for type I PDT.

Photostability is a critical parameter for the practical application of phototherapeutic agents. Compared with ICG (a clinically used NIR dye), both OOH and SOH displayed more excellent photostability (Fig. 1l and S11). This result was attributed to the higher structural rigidity of the two dyes, which could resist photoinduced oxidative degradation and structural damage. Under 808 nm laser irradiation, the temperature of OOH aqueous solution increased slowly (Fig. 1m), while the temperature of SOH aqueous solution increased rapidly with prolonged irradiation time (Fig. 1n). The PCE of OOH was 26.1% (Fig. 1o), whereas that of SOH reached as high as 42.3% (Fig. 1p). These findings indicated that the introduction of a sulfur atom into NIR-II xanthene dyes could red-shift the absorption/emission spectra, enhance the molar extinction coefficient, reduce the fluorescence quantum yield and brightness, eliminate the generation of oxygen-dependent type II ROS ($^1O_2$), strengthen the production of oxygen-independent type I ROS ($O_2{}^{\bullet-}$ and $^{\bullet}$OH), and improve the PCE. These properties were conducive to combating hypoxic tumors through oxygen-independent type I PDT and PTT.

The regulatory mechanism of sulfur atom incorporation on the photophysical properties and photochemical reactions of dye SOH

We further employed density functional theory (DFT) calculations to reveal the intrinsic mechanism underlying the differences in photophysical properties, ROS generation, and photothermal performance between OOH and SOH. As shown in Fig. 2a, the highest occupied molecular orbital (HOMO) energy level of OOH was −7.68 eV, the lowest unoccupied molecular orbital (LUMO) energy level was −5.64 eV, and the energy gap (E_{gap}) was 2.04 eV. In contrast, the HOMO and LUMO energy levels of SOH were −7.63 eV and −5.66 eV, respectively, with a narrowed E_{gap} of 1.97 eV (Fig. 2b). According to the energy gap law, E_{gap} was negatively correlated with the absorption/emission wavelength. The narrower E_{gap} of SOH directly led to a significant red-shift of its absorption (679–888 nm) and emission (919–983 nm) wavelengths compared to OOH (λ_{abs}: 654–857 nm; λ_{em}: 855–935 nm) (Fig. 1a–d, Tables 1 and 2). Fig. 2c shows that the dihedral angle between the two symmetric xanthene moieties of OOH was 20.5°, with only slight distortion of the conjugated skeleton (Fig. S11). In contrast, due to the presence of a thioxanthene moiety on one side, the dihedral angle between the xanthene/thioxanthene moieties of SOH increased to 31.2°, resulting in a significantly more twisted conjugated skeleton (Fig. 2d and S12). The sulfur atom had a larger atomic radius and lower electronegativity than the oxygen atom, which increased the distortion of the molecular skeleton, intensified intramolecular rotation and vibration, and facilitated the dissipation of excited-state energy through non-radiative transitions.[56,57] This competed with the fluorescence emission, directly leading to a decrease in fluorescence quantum yield (Tables 1 and 2). In addition, the energy generated by non-radiative transitions was not released in the form of photons but converted into molecular thermal motion, thereby improving the PCE (Fig. 1m–p and Table 3).

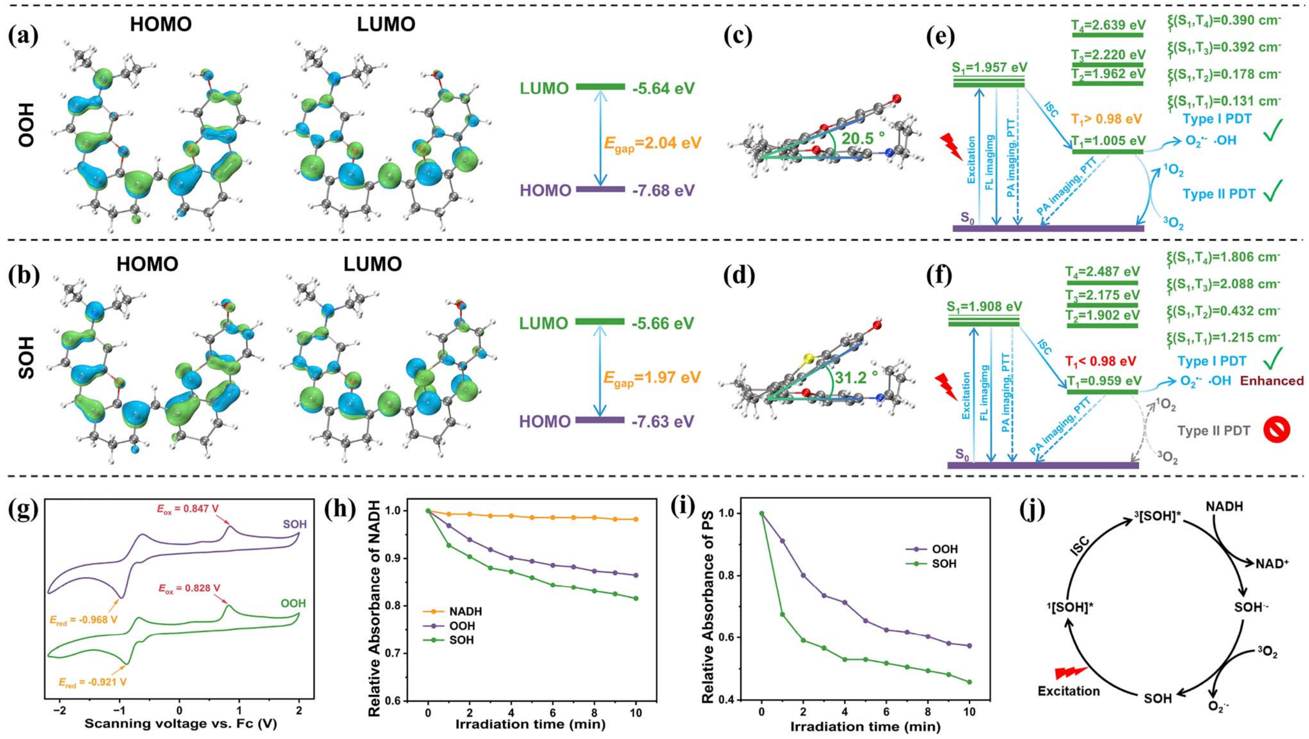

Fig. 2 (a) HOMO, LUMO, and corresponding energy gap (E_{gap}) of OOH. (b) HOMO, LUMO, and corresponding energy gap (E_{gap}) of SOH. (c) Dihedral angle between the two xanthene moieties of OOH in the optimal geometric configuration. (d) Dihedral angle between the xanthene/thioxanthene moieties of SOH in the optimal geometric configuration. (e) Lowest singlet state energy level (S_1), triplet state energy levels (T_1–T_4), spin–orbit coupling constants ($\xi(S_1, T_n)$), and Jablonski diagram illustrating the fluorescence emission, ROS ($^1O_2$, $O_2^{•-}$, and $^•OH$) generation, and heat production of OOH. (f) Lowest singlet state energy level (S_1), triplet state energy levels (T_1–T_4), spin–orbit coupling constants ($\xi(S_1, T_n)$), and Jablonski diagram illustrating the fluorescence emission, type I ROS generation, and heat production of SOH. (g) Cyclic voltammetry curves of OOH and SOH. (h) Absorption degradation curves of NADH in the absence or presence of OOH and SOH, respectively. (i) Absorption degradation curves of OOH and SOH in the presence of NADH. (j) Proposed mechanism for $O_2^{•-}$ generation by SOH under laser irradiation.

Table 3 Calculations of the intersystem crossing rate and Gibbs free energy for the electron transfer process of OOH and SOH

Dye	$\xi(S_1, T_1)$ [cm^{-1}]	ΔE_{S1T1} [eV]	R^a [× 10^9]	$E_{OX}{}^b$ [V]	ΔG [kJ mol^{-1}]	PCE
OOH	0.131	0.952	0.291	0.918	−10.903	26.1%
SOH	1.215	0.949	25.163	0.937	−17.174	42.3%

[a] $k_{ISC} \propto R = [\xi(S_1, T_1)/\Delta E_{S1T1}]^2$. [b] E_{OX} was the oxidation potential of dyes *versus* NHE.

Combined with the excited state energy level diagrams (Fig. 2e and f and S13), spin–orbit coupling constants ($\xi(S_1, T_n)$), and quantitative calculations in Tables 3 and S1–S4, the differences in the type and efficiency of ROS generation between OOH and SOH could be accurately explained from the perspective of excited-state relaxation pathways. Intersystem crossing (ISC) is a key process connecting the singlet and triplet states, and its efficiency directly determines the competitive relationship between fluorescence quenching, ROS generation, and photothermal conversion. As shown in Fig. 2e–f and Table 3, the $\xi(S_1, T_1)$ value of SOH (1.215 cm^{-1}) was 9.3-fold that of OOH (0.131 cm^{-1}), and the ISC rate-related parameter R (25.163 × 10^9) was 86.5-fold that of OOH (0.291 × 10^9). This difference originated from the heavy atom effect of sulfur and more twisted molecular backbone of SOH. Sulfur has a higher atomic number than oxygen, and the stronger spin–orbit coupling effect significantly improved the ISC efficiency of SOH from the lowest singlet state (S_1) to the lowest triplet state (T_1), resulting in more excited-state electrons being distributed to the triplet state instead of emitting fluorescence through radiative transitions.[34] We characterized the triplet-state lifetimes of the two dyes using a transient absorption spectrometer. The triplet-state lifetime of OOH was 47 ns, while that of SOH was 68 ns (Fig. S14). Benefiting from its longer triplet-state lifetime, SOH exhibited higher efficiency in generating ROS. This also explained the experimental phenomenon that the fluorescence quantum yield of SOH (maximum 0.09%) was much lower than that of OOH (maximum 0.36%) (Tables 1 and 2). The type of ROS generation (type I/type II) was directly determined based on the energy difference between the T_1 level and the triplet-to-singlet transition of oxygen molecules (0.98 eV). The T_1 level of OOH was 1.005 eV (>0.98 eV), which could sensitize oxygen molecules to $^1O_2$ through energy transfer. Meanwhile, some triplet states of OOH could generate type I ROS through electron transfer, which was consistent with the simultaneous detection of $^1O_2$, $O_2^{\bullet-}$, and $^{\bullet}OH$ from OOH under laser irradiation as shown in Fig. 1e–k. Interestingly, the introduction of a sulfur atom reduced the T_1 level of SOH to 0.959 eV (<0.98 eV), which was insufficient to sensitize oxygen to $^1O_2$, thus preventing type II PDT.[21,22] However, its high ISC efficiency led to the accumulation of electrons in the T_1 state. Moreover, the Gibbs free energy change (ΔG) for electron transfer of SOH (−17.174 kJ mol^{-1}) was more negative than that of OOH (−10.903 kJ mol^{-1}) (Table 3), making the electron transfer reaction more spontaneous and thereby efficiently generating type I ROS (Fig. 1e–k).[13,34] In addition, the more twisted molecular backbone of SOH conferred upon it a large SOC matrix element, which promoted the SOCT-ISC process and thereby facilitated the generation of type I ROS.[23,31,35]

The cyclic voltammetry (CV) and NADH degradation experiments of OOH and SOH further revealed the differences in their type I ROS generation efficiency. Combined with the CV curves (Fig. 2g) and Table 3, the oxidation potential (E_{OX}) of SOH was 0.937 V (*vs.* NHE), slightly higher than that of OOH (0.918 V), indicating that SOH had stronger oxidizing ability. Thus, under laser irradiation, the degradation rate of NADH by SOH was significantly higher than that by OOH (Fig. 2h and S15a–c), and the degradation of the absorption spectra of SOH was also greater than that of OOH (Fig. 2i and S15a–c). The degradation of the absorption spectra of the two dyes was not due to structural decomposition under light irradiation; in fact, both dyes exhibited excellent photostability (Fig. 1l). Instead, during the conversion of NADH to NAD^+, the triplet state of SOH ($^3[SOH]^*$) obtained electrons and was converted to $SOH^{\bullet-}$, leading to the destruction of the conjugated structure and a decrease in the absorption spectra (Fig. 2j and S15d).[58,59] $SOH^{\bullet-}$ sensitized oxygen to generate $O_2^{\bullet-}$ through electron transfer, and the $O_2^{\bullet-}$ further generated $^{\bullet}OH$ through the Haber Weiss reaction, while oxygen was recycled (Fig. S16).[10,60] Therefore, the generation of type I ROS by SOH under laser irradiation was oxygen-independent. This property, combined with the more negative ΔG, further verified that the electron transfer-driven type I ROS generation efficiency of SOH was superior to that of OOH.

Non-radiative transition of the excited-state was the core of photothermal conversion. The high ISC efficiency of SOH caused a large number of S_1-states to transfer to the T_1 states. Due to the low T_1 level and spontaneous electron transfer reaction ($\Delta G < 0$) of SOH, some T_1-states generated type I ROS through electron transfer, while the remaining T_1-states released heat through non-radiative transitions such as vibrational relaxation. Meanwhile, the molecular conjugation distortion induced by the introduction of sulfur atoms further promoted non-radiative transitions (inhibiting fluorescence emission), converting more light energy into heat. In contrast, OOH had low ISC efficiency, and most of the S_1-states emitted fluorescence through radiative transitions, resulting in a low proportion of non-radiative transitions and thus a low PCE (26.1%). The more efficient type I ROS generation and higher PCE (42.3%) of SOH were beneficial for combating hypoxic tumors through oxygen-independent type I PDT and PTT.

Aggregation behavior of dye SOH and the formation mechanism of J_{CT}-aggregates induced by phosphates

Due to its excellent photophysical properties, reactive oxygen species (ROS) generation capability, and photothermal effect, SOH was employed for subsequent tumor diagnosis and therapy. When attempting to investigate the pH stability of SOH, the dye was dissolved in PBS with different pH values (2–11) using THF as a co-solvent (volume ratio: 0.2%). Excitingly, an unexpected aggregation peak at approximately 1100 nm appeared when the pH ranged from 6 to 11 (Fig. 3a). We further investigated the effect of THF/PBS volume ratio on the aggregation behavior of SOH and found that as the volume ratio of THF increased from 0.2% to 100%, the position of the aggregation peak exhibited a regular shift, and the peak shape gradually broadened from sharp (Fig. 3b). When the proportion of THF exceeded 15%, the aggregation peak almost disappeared. More interestingly, when SOH was added to THF/H_2O mixed solvents with different volume ratios, no aggregation peak was observed within the THF volume ratio range of 0.2–100% (Fig. 3c). Similar conclusions were obtained when DMSO was used as the co-solvent (Fig. S17). We further studied the time dependence of the aggregation behavior of SOH. It was found that SOH aggregated immediately upon being added to PBS, and the aggregation peak reached a plateau within 10 min (Fig. 3d and e). In contrast, when SOH was added to water, no new aggregation peak was observed even after extending the time to 30 min (Fig. 3f and g). Consistent results were also achieved with DMSO as the co-solvent (Fig. S18). For comparison, the aggregation behavior of OOH was also investigated. A similar *J*-aggregate absorption peak at 982 nm was observed for OOH in PBS with pH ranging from 5.5 to 11 (Fig. S19a). The aggregation properties of OOH in PBS and water were further explored. Within the DMSO volume ratio of 0.2% to 30%, OOH exhibited stronger *J*-aggregate absorption peaks and faster aggregation kinetics in PBS than in water (Fig. S19b, c and S20). In the DMSO volume ratio range of 0.2% to 1%, weak *J*-aggregate absorption peaks were detected for OOH in water, which was probably attributed to the higher electronegativity of O compared with S. As shown in Fig. 3h, compared to the SOH monomer (886 nm), a distinct red-shifted absorption peak at 1110 nm and a blue-shifted shoulder peak at 848 nm emerged when SOH was dissolved in PBS, which represented the characteristic absorption spectrum of CT-coupled *J*-aggregates.[35–38] However, when SOH was dissolved in water, the absorption peak was blue-shifted to 712 nm. Under excitation with a 1064 nm laser, the fluorescence peak of SOH in PBS was significantly red-shifted to 1132 nm with enhanced fluorescence (22.6-fold), while almost no emitted fluorescence was detected when SOH was in water (Fig. 3i). When SOH was placed in PBS with different pH values, the NIR-II fluorescence intensity in the pH range of 6–11 was higher than that in the range of 2–5.5, and the highest NIR-II fluorescence intensity was achieved at pH 6–7

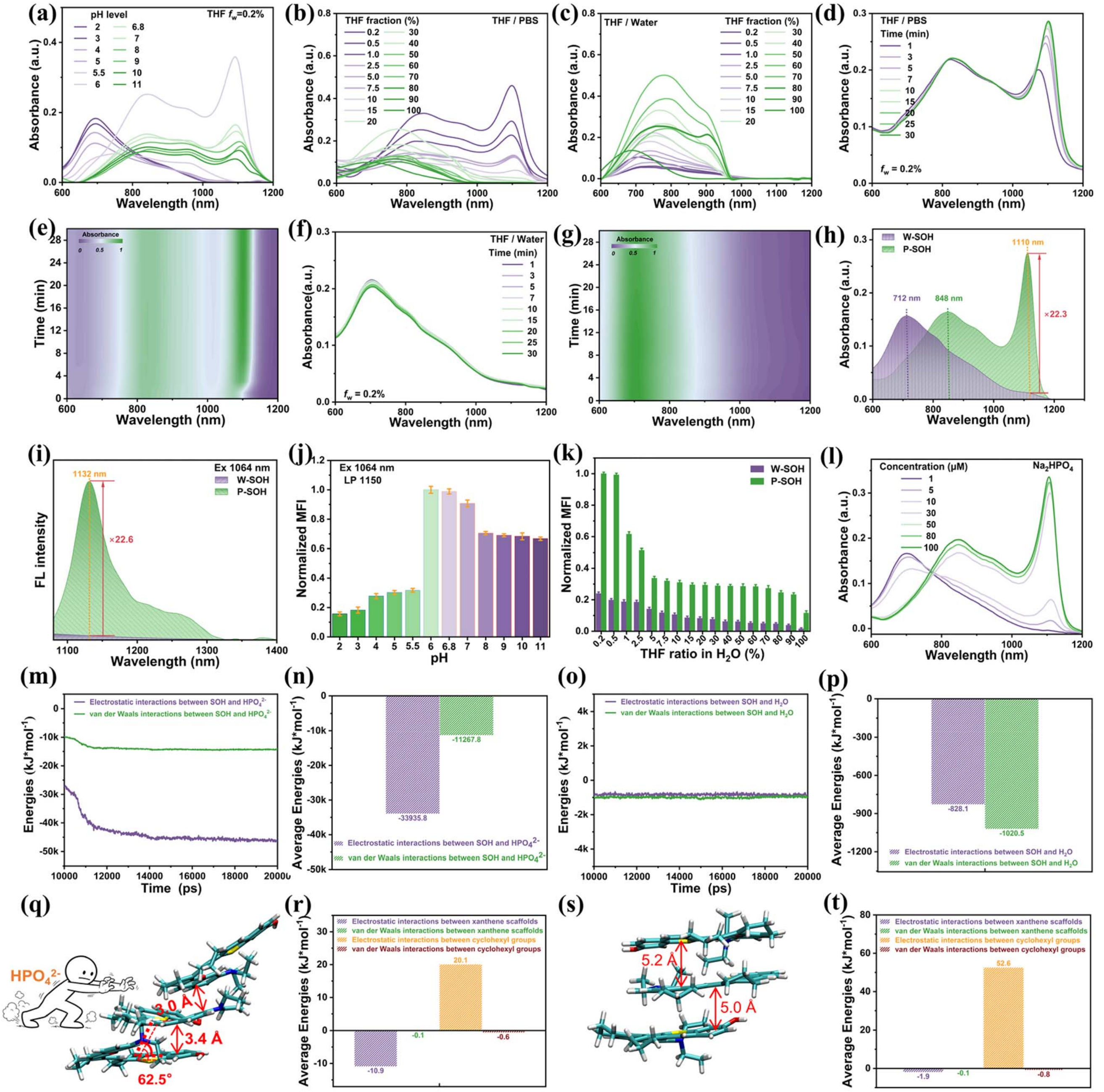

Fig. 3 (a) Changes in the absorption spectra of SOH in PBS with different pH values (THF volume ratio: 0.2%). (b) Changes in the absorption spectra of SOH in THF/PBS mixed solvents (THF volume ratio: 0.2–100%). (c) Changes in the absorption spectra of SOH in THF/water mixed solvents (THF volume ratio: 0.2–100%). (d) and (e) Time-dependent changes in the absorption spectra of SOH in THF/PBS mixed solvent. (f) and (g) Time-dependent changes in the absorption spectra of SOH in THF/water mixed solvent. (h) Absorption spectra of SOH in water and PBS, respectively. (i) Fluorescence spectra of SOH in water and PBS, respectively; excitation wavelength: 1064 nm. (j) Changes in the NIR-II fluorescence intensity of SOH in PBS with different pH values (excitation: 1064 nm, LP 1150 nm). (k) Changes in the NIR-II fluorescence intensity of SOH in THF/PBS or THF/water mixed solvents (THF volume ratio: 0.2–100%) (excitation: 1064 nm, LP 1150 nm). (l) Changes in the absorption spectra of SOH in Na_2HPO_4 solutions with different concentrations. (m) Changes in the interaction energy between SOH and HPO_4^{2-} from molecular dynamics simulations. (n) Average interaction energy between SOH and HPO_4^{2-} from molecular dynamics simulations. (o) Changes in the interaction energy between SOH and water from molecular dynamics simulations. (p) Average interaction energy between SOH and water from molecular dynamics simulations. (q) Packing mode of SOH induced by HPO_4^{2-}. (r) Average interaction energy of the xanthene skeletons (or cyclohexyl groups) between SOH molecules induced by HPO_4^{2-}. (s) Packing mode of SOH induced by water. (t) Average interaction energy of the xanthene skeletons (or cyclohexyl groups) between SOH molecules induced by water.

(Fig. 3j and S21). The NIR-II fluorescence intensity of SOH in THF/PBS mixed solvents with different volume ratios was significantly higher than that in THF/H_2O mixed solvents, and the NIR-II fluorescence intensity gradually increased with the decrease in THF proportion (Fig. 3k and S22). PBS is composed of Na_2HPO_4, KH_2PO_4, KCl, and NaCl. We further investigated the effects of different components in PBS on the aggregation behavior of SOH. It was found that SOH could only undergo such aggregation under the induction of Na_2HPO_4, resulting in an absorption peak similar to that in PBS (Fig. 3l), while other components had no effect (Fig. S23). In addition, we verified that this aggregation was not induced by H^+ in weakly acidic pH solutions, and no aggregation peak appeared when SOH was added to solutions with pH 6–7 adjusted with dilute hydrochloric acid (Fig. S24). We also confirmed that this aggregation was irrelevant to Na^+, as K_2HPO_4 and $(NH_4)_2HPO_4$ were also effective. Furthermore, hydrolysis of PO_4^{3-} mainly produces HPO_4^{2-}, and PO_4^{3-} was also effective (Fig. S25a). Some inorganic salts (PO_3^{2-}, SO_3^{2-}, and CO_3^{2-}) that could hydrolyze to form ions with similar structures to that of HPO_4^{2-} or HCO_3^- were also effective (Fig. S25a and b).

We further utilized molecular dynamics (MD) simulations (Fig. S26) to reveal the core mechanism underlying the regulation of SOH aggregation by HPO_4^{2-} at the molecular level, wherein HPO_4^{2-} induced offset stacking of SOH molecules through electrostatic interaction. The interaction energy between SOH and HPO_4^{2-} continuously decreased during the simulation (Fig. 3m), with an average electrostatic interaction energy of −33935.8 kJ mol^{-1} and an average van der Waals interaction energy of −11267.8 kJ mol^{-1} (Fig. 3n). In contrast, the interaction energy between SOH and H_2O remained almost unchanged during the simulation (Fig. 3o), with an average electrostatic interaction energy of −828.1 kJ mol^{-1} and an average van der Waals interaction energy of −1020.5 kJ mol^{-1}, which were significantly lower than those between SOH and HPO_4^{2-}. Therefore, there existed a stable and strong attractive interaction (mainly electrostatic interaction) between SOH and HPO_4^{2-}. Combined with the electrostatic potential map of SOH (Fig. S27), the positively charged regions (xanthene skeleton) on the molecular surface formed a precise match with the negatively charged sites of HPO_4^{2-}, thereby inducing offset stacking of SOH molecules. Upon induction by HPO_4^{2-}, SOH molecules displayed moderate slipped π–π stacking and a reduced intermolecular distance of 3.0–3.4 Å that enlarged intermolecular orbital overlap and promoted intermolecular charge transfer, and the slip angle was determined to be 62.5°, an angle larger than 54.7° for conventional *J*-aggregates, which confirmed the characteristic features of CT-coupled *J*-aggregates (Fig. 3q and S26c).[35–38] In contrast, under the induction of water, SOH molecules were in a disordered dispersion state, with the intermolecular distance greater than 5.0 Å (Fig. 3s and S26f). This difference originated from the inductive effect of HPO_4^{2-}: HPO_4^{2-} broke the intermolecular hydrophobic repulsion through electrostatic interaction with SOH, promoting offset aggregation. Under the induction of HPO_4^{2-}, the average electrostatic interaction energy of the xanthene skeletons between SOH molecules was −10.9 kJ mol^{-1}, and the average van der Waals interaction energy of the cyclohexyl groups between SOH molecules was 20.1 kJ mol^{-1} (Fig. 3r and S28a). In contrast, under the induction of water, the average electrostatic interaction energy of the xanthene skeletons between SOH molecules decreased to −1.9 kJ mol^{-1}, and the average van der Waals interaction energy of the cyclohexyl groups between SOH molecules increased to 52.6 kJ mol^{-1} (Fig. 3t and S28b). These results demonstrated that under the induction of HPO_4^{2-}, the average electrostatic interaction energy of the xanthene skeletons between SOH molecules was more negative (stronger electrostatic attraction), and the average van der Waals interaction energy of the cyclohexyl groups between SOH molecules was smaller. This demonstrated that HPO_4^{2-}-driven electrostatic interactions among SOH molecules and HPO_4^{2-} led to the formation of CT-coupled *J*-aggregates. Compared with monomers, their absorption/emission spectra were significantly red-shifted (λ_{abs} = 1110 nm; λ_{em} = 1132 nm) with enhanced fluorescence (22.6-fold) (Fig. 3h and i). In contrast, under the induction of water, the average electrostatic interaction energy of the xanthene skeletons between SOH molecules was almost zero (the distance was too large for electrostatic attraction to occur), and the average van der Waals interaction energy of the cyclohexyl groups between SOH molecules was larger. This indicated that SOH molecules tended to undergo vertical disordered stacking, with an absorption spectrum (λ_{abs} = 712 nm) comparable to that of monomers. Meanwhile, the absorbance at 1064 nm was almost zero, and almost no fluorescence was emitted under irradiation with a laser of this wavelength (Fig. 3h and i).

Photophysical properties, reactive oxygen species generation, and photothermal performance of P-SOH NPs

Benefiting from the impressive photophysical properties of the CT-coupled *J*-aggregates of SOH induced by HPO_4^{2-}, we encapsulated the J_{CT}-aggregates using the amphiphilic polymer F127, and the resulting nanoparticles were named P-SOH NPs. Meanwhile, as a control, nanoparticles prepared in water were denoted as W-SOH NPs. As shown in Fig. 4a, the absorption spectrum of W-SOH NPs (absorption peak at 766 nm) was comparable to that of SOH monomers, while P-SOH NPs displayed a pronounced red-shifted absorption peak at 1120 nm (redshifted by 354 nm) alongside a weakly blue-shifted shoulder peak at 858 nm, which preserved the characteristic absorption features of CT-coupled *J*-aggregates. Under excitation with a 1064 nm laser, the NIR-II fluorescence peak of P-SOH NPs was remarkably red-shifted to 1134 nm, whereas W-SOH NPs exhibited almost no fluorescence emission (Fig. 4b), indicating that the CT-coupled *J*-aggregates of P-SOH NPs was more favorable for fluorescence emission (enhanced 36.1-fold). Fig. 4c and S29 show that the hydrodynamic diameter obtained from dynamic light scattering (DLS) of W-SOH NPs was 85 nm, and that of P-SOH NPs was 75 nm, both falling within the 10–200 nm range suitable for *in vivo* circulation. Combined with the TEM images in the insets of Fig. 4c, the sizes of W-SOH NPs and P-SOH NPs were 81 nm and 73 nm, respectively, which were slightly smaller than their hydrodynamic diameters due to the shrinkage of the hydration layer after drying. The zeta potential of W-SOH NPs was 0.38 mV, and that of P-SOH NPs was 0.34 mV (Fig. 4d).

Under 1064 nm laser irradiation, the two types of nanoparticles exhibited significant differences in the type and efficiency of ROS generation. Notably, the ROS generation

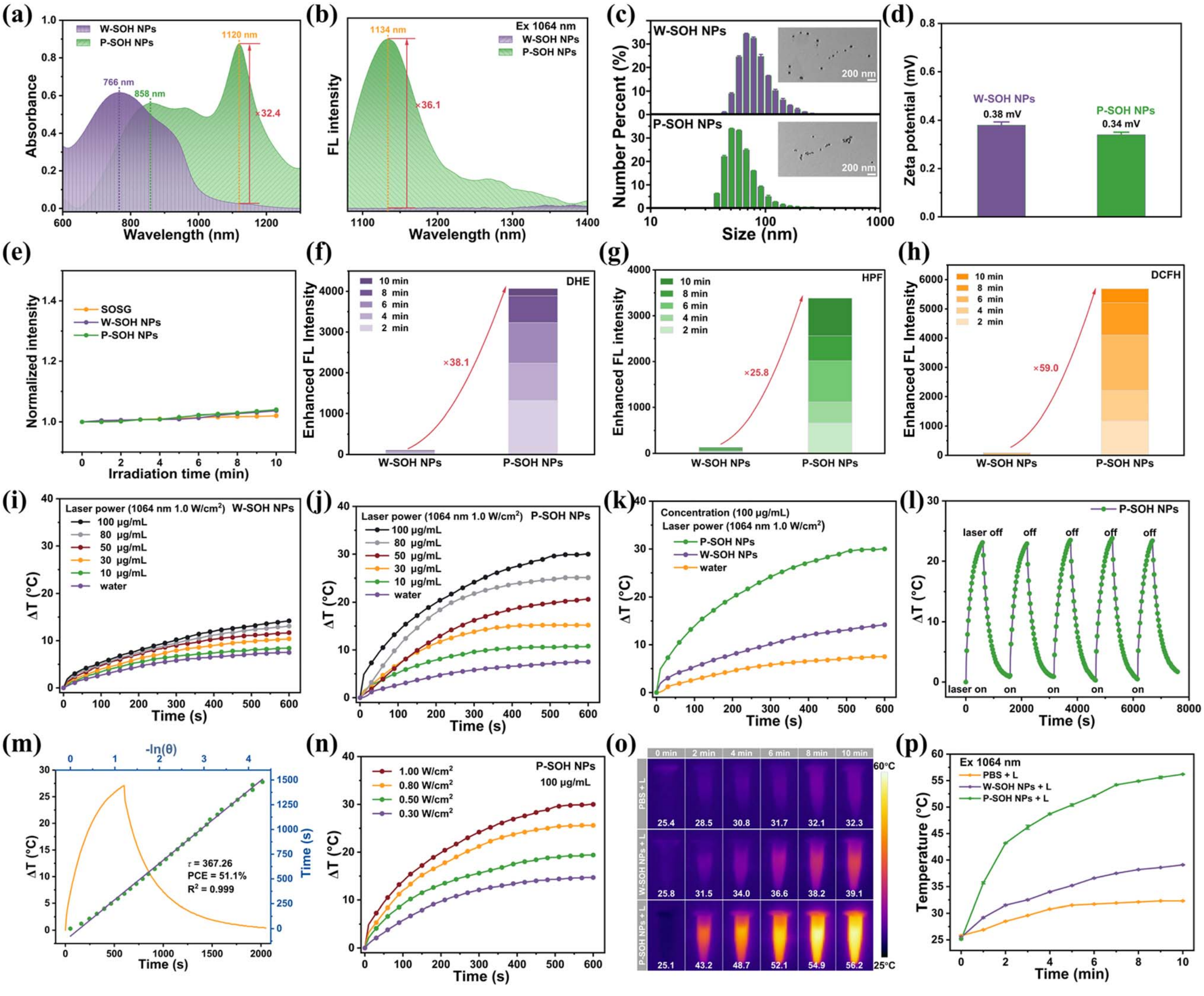

Fig. 4 (a) Absorption spectra of W-SOH NPs and P-SOH NPs. (b) Fluorescence spectra of W-SOH NPs and P-SOH NPs under 1064 nm laser excitation. (c) Hydrodynamic diameters of W-SOH NPs and P-SOH NPs; insets show the corresponding TEM images. (d) Zeta potentials of W-SOH NPs and P-SOH NPs. The following tests were all performed under 1064 nm laser irradiation. Evaluation of (e) $^1O_2$, (f) $O_2^{\bullet-}$, (g) $^{\bullet}OH$, and (h) total ROS generation capabilities of W-SOH NPs and P-SOH NPs, respectively. (i) Photothermal effects of W-SOH NPs at different concentrations. (j) Photothermal effects of P-SOH NPs at different concentrations. (k) Comparison of photothermal effects between W-SOH NPs and P-SOH NPs. (l) Photothermal stability of P-SOH NPs during five laser on–off cycles. (m) Evaluation of the photothermal conversion efficiency of P-SOH NPs. (n) Photothermal effects of P-SOH NPs under laser irradiation at different powers. (o) Photothermal images of W-SOH NPs and P-SOH NPs, and water as a control. (p) Temperature change trends at different time points in (o).

capacity of P-SOH NPs was further enhanced, inheriting the advantage of SOH monomers in producing type I ROS. As shown in Fig. 4e and S30, no obvious $^1O_2$ generation signal was detected for either nanoparticle using the SOSG probe, which was consistent with the characteristic of SOH monomers being unable to generate type II ROS. This confirmed that the nanonization process did not alter their ROS generation type, and type I ROS remained the dominant species. Tests with $O_2^{\bullet-}$ (Fig. 4f and S31) and $^{\bullet}OH$ (Fig. 4g and S32) probes demonstrated that the fluorescence enhancement rates of P-SOH NPs was 38.1-fold and 25.8-fold that of W-SOH NPs, respectively. In the total ROS detection (Fig. 4h and S33), the DCFH fluorescence intensity of P-SOH NPs reached 59.0-fold that of W-SOH NPs after 10 min of irradiation. This difference originated from the superior 1064 nm laser harvesting efficiency of P-SOH NPs, which facilitated the transfer of excited-state electrons to generate type I ROS more efficiently, providing a core foundation for type I PDT of hypoxic tumors. Moreover, the ROS generation efficiency of aggregated OOH in PBS and water was comparatively analyzed. The results revealed that OOH *J*-aggregates formed in PBS also exhibited higher production efficiencies of $^1O_2$ (Fig. S34), $O_2^{\bullet-}$ (Fig. S35), $^{\bullet}OH$ (Fig. S36), and total ROS (Fig. S37).

Subsequently, we further investigated the differences in photothermal effects between W-SOH NPs and P-SOH NPs. As shown in Fig. 4i, only a weak photothermal effect was observed with increasing concentrations of W-SOH NPs. In contrast, P-SOH NPs exhibited a more significant temperature increase (Fig. 4j). At a concentration of 100 μg mL^{-1}, the equilibrium temperature of P-SOH NPs reached 55 °C, an increase of 30 °C compared to the initial temperature, while W-SOH NPs only showed a 14.2 °C increase (Fig. 4k). Fig. 4l shows that during five laser on–off cycles, the deviation in the equilibrium temperatures of P-SOH NPs after each irradiation was less than 2 °C, and the photothermal curves almost overlapped completely, demonstrating excellent photothermal cycling stability. As presented in Fig. 4m, the PCE of P-SOH NPs reached 51.1%. This high PCE was attributed to the efficient light absorption of P-SOH NPs, which converted more light energy into heat through non-radiative transitions. Fig. 4n shows that the photothermal effect of P-SOH NPs was significantly enhanced with increasing laser power (0.3–1.0 W cm^{-2}). This distinct power dependence enabled precise regulation of PTT, allowing adaptation to tumors of different sizes and depths by adjusting the laser power. Photothermal images (Fig. 4o) and temperature change curves (Fig. 4p) intuitively demonstrated that at the same concentration and laser power, P-SOH NPs exhibited the fastest temperature increase rate, reaching 56.2 °C after 10 min of irradiation; in contrast, W-SOH NPs only reached 39.1 °C, and that of the water control group only increased to 32.3 °C. Thus, P-SOH NPs exhibited a more prominent photothermal effect. Therefore, P-SOH NPs integrated strong NIR-II absorption, efficient type I ROS generation, a high PCE of 51.1%, and excellent photothermal stability. They perfectly combined type I PDT and PTT, both of which are oxygen-independent, making them suitable for the phototherapy of hypoxic tumors.

Verification of oxygen-independent phototoxicity of P-SOH NPs at the cellular level

Cytotoxicity assays (under normoxic or hypoxic conditions) confirmed the biocompatibility and phototoxicity of W-SOH NPs and P-SOH NPs, with P-SOH NPs exhibiting superior phototoxicity even in hypoxic environments. In the absence of laser irradiation (Fig. 5a), both W-SOH NPs and P-SOH NPs maintained a cell viability of nearly 100% within the concentration range of 0.5–10 μg mL^{-1}, with no significant decrease as the concentration increased, indicating that both nanoparticles possessed excellent biocompatibility. After irradiation with a 1064 nm laser (Fig. 5b), the phototoxicity of P-SOH NPs showed a distinct concentration dependence and was not affected by the oxygen environment. Under both normoxic and hypoxic conditions, the cell viability decreased to less than 20% at a concentration of 10 μg mL^{-1}. In contrast, W-SOH NPs exhibited negligible phototoxicity, with a cell viability higher than 90% at the same concentration. This difference directly originated from the performance differentiation of the two nanoparticles: P-SOH NPs featured a high PCE (51.1%) and efficient generation of type I ROS, both of which were oxygen-independent. However, W-SOH NPs had weak light absorption, low ROS generation efficiency, and poor PCE, resulting in almost no phototoxicity.

Intracellular ROS probe staining experiments directly verified the type and efficiency of ROS generation by P-SOH NPs at the cellular level, clarifying the core mechanism of their oxygen-independent therapy. As shown in Fig. 5e, no obvious fluorescence signal was detected in all groups using the SOSG probe ($^1O_2$-specific), confirming that neither nanoparticle could generate type II ROS in cells. In contrast, the P-SOH NPs + L group (with laser irradiation) exhibited strong fluorescence signals in DHE ($O_2^{\bullet-}$-specific), HPF ($^{\bullet}OH$-specific), and DCFH (total ROS-specific) probe staining under both normoxic and hypoxic conditions, and the fluorescence intensity under hypoxia was not significantly different from that under normoxia. Conversely, the W-SOH NPs + L group showed almost no fluorescence signal in ROS probe staining. These results indicated that P-SOH NPs could efficiently generate type I ROS in cells without relying on oxygen, while W-SOH NPs had almost no ability to generate ROS. Thus, P-SOH NPs were expected to achieve efficient phototherapy of hypoxic tumors.

Flow cytometric apoptosis analysis and calcein-AM/PI staining confirmed the efficient phototherapeutic efficacy of P-SOH NPs at the cellular level, which maintained the advantage of synergistic therapy even in hypoxic environments. Flow cytometric apoptosis analysis (Fig. 5c and g) showed that in the P-SOH NPs + L group (with laser irradiation), the proportion of late apoptotic cells exceeded 95% under both normoxic and hypoxic conditions; in contrast, the W-SOH NPs + L group showed almost no cell apoptosis. The proportion of apoptotic cells in the PBS groups (with or without a laser) and non-laser groups was less than 5%, excluding cell damage caused by the laser itself or the nanoparticles. The calcein-AM/PI staining images (Fig. 5d and f) were consistent with the flow cytometric data. In the P-SOH NPs + L group (in both normoxic and hypoxic environments), the proportion of red fluorescence (dead cells) in the field of view was significantly higher than that in other groups, with the proportion of live cells (green fluorescence) less than 20%, while green fluorescence remained dominant in the W-SOH NPs + L group. This intuitive result confirmed that the phototherapeutic efficacy of P-SOH NPs led to strong hypoxia resistance. Therefore, P-SOH NPs could efficiently induce tumor cell apoptosis through the synergistic effect of type I PDT and PTT, and this process was not inhibited by the hypoxic tumor microenvironment.

High-resolution NIR-II fluorescence/photoacoustic tumor angiography of P-SOH NPs

In vitro experiments clarified the NIR-II fluorescence imaging properties of W-SOH NPs and P-SOH NPs. Benefiting from the fluorescence red-shift and enhancement effects of CT-coupled *J*-aggregates, P-SOH NPs exhibited significantly superior imaging performance compared to W-SOH NPs. As shown in Fig. 6a, under 1064 nm laser excitation, the NIR-II fluorescence imaging signal of P-SOH NPs increased obviously with the increase in concentration, while W-SOH NPs showed almost no significant fluorescence imaging effect at the same concentration. The quantitative intensities in Fig. 6b further confirmed that the NIR-II fluorescence intensity of P-SOH NPs was significantly

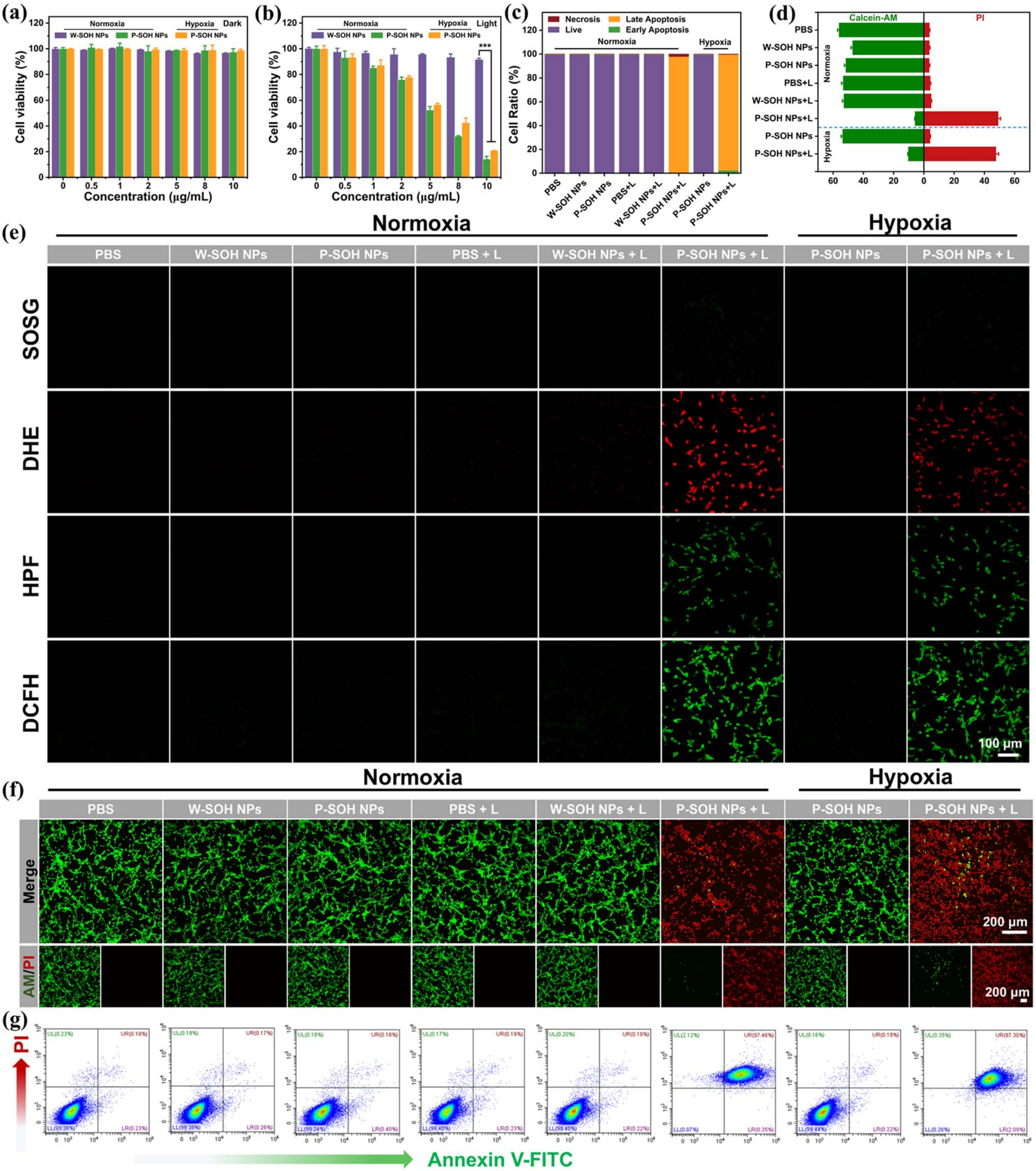

Fig. 5 Verification of the phototoxicity of P-SOH NPs at the cellular level under normoxic or hypoxic conditions. (a) Dark toxicity of W-SOH NPs and P-SOH NPs. (b) Phototoxicity of W-SOH NPs and P-SOH NPs. $^{***}p < 0.001$. (c) Statistical proportion of cells at different apoptotic stages after various treatments. (d) Statistical proportion of live/dead cells after various treatments. (e) Intracellular generation of $^1O_2$ (SOSG probe), $O_2^{\bullet -}$ (DHE probe), $^{\bullet}OH$ (HPF probe), and total ROS (DCFH probe) in each group after various treatments. (f) Calcein-AM/PI staining images of cells in each group after various treatments. (g) Apoptotic proportion of cells in each group after various treatments.

higher than that of W-SOH NPs. This difference originated from the molecular packing modes of the two nanoparticles: P-SOH NPs formed CT-coupled *J*-aggregates *via* offset stacking induced by HPO_4^{2-}, which significantly improved the NIR-II fluorescence emission efficiency. In contrast, W-SOH NPs were randomly dispersed in water, leading to severe fluorescence quenching. Fig. 6c shows that under the same 1064 nm excitation and concentration, the imaging clarity and signal

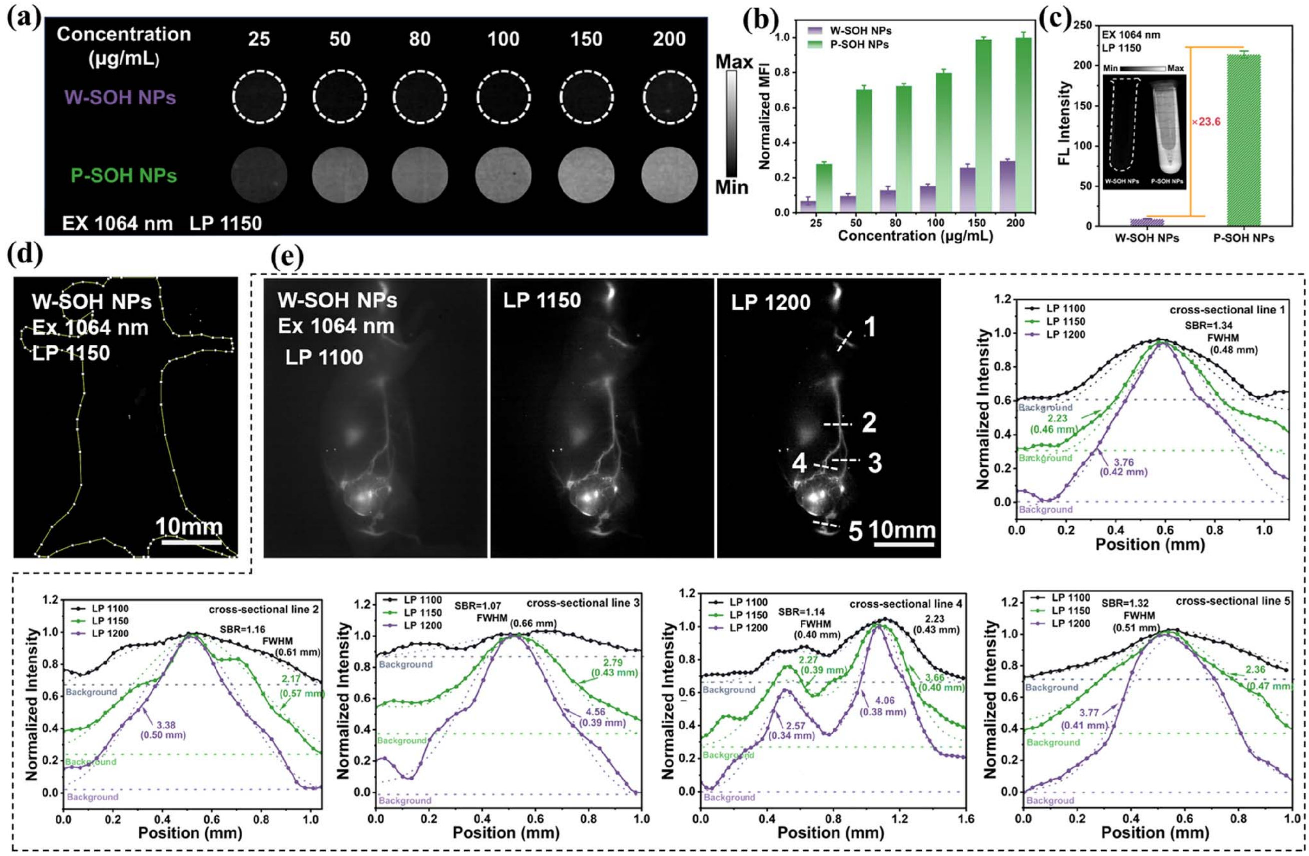

Fig. 6 (a) NIR-II fluorescence images of W-SOH NPs and P-SOH NPs at different concentrations. (b) Quantification of NIR-II fluorescence intensities of W-SOH NPs and P-SOH NPs at different concentrations. (c) Comparison of NIR-II fluorescence imaging capabilities between W-SOH NPs and P-SOH NPs. (d) NIR-II fluorescence image of mice after tail vein injection of W-SOH NPs. (e) NIR-II fluorescence images and tumor angiography analysis of mice after tail vein injection of P-SOH NPs under long-pass filters LP1100, LP1150, and LP1200, respectively.

intensity of P-SOH NPs (enhanced 23.6-fold) in the NIR-II window (LP1150 filter) were far superior to those of W-SOH NPs. After tail vein injection of W-SOH NPs, no obvious NIR-II fluorescence signal was observed in the whole body of mice (Fig. 6d). In contrast, tumor angiogenesis imaging was achievable in mice injected with P-SOH NPs under different long-pass filters (LP1100, LP1150, and LP1200) (Fig. 6e). The tumor angiography analysis of P-SOH NPs (Fig. 6e) demonstrated that they could clearly distinguish the microvessels of tumors. Moreover, as the wavelength of the long-pass filter increased, the tumor angiographic resolution improved, with the minimum full width at half maximum (FWHM) of blood vessels reaching 0.34 mm and the signal-to-background ratio (SBR) as high as 4.56.

In addition, *in vitro* experiments confirmed that there was a significant difference in the NIR-II photoacoustic imaging performance between W-SOH NPs and P-SOH NPs. With a significantly red-shifted NIR-II absorption peak, P-SOH NPs exhibited a concentration-dependent photoacoustic signal enhancement effect. As shown in Fig. 7a, under 1064 nm laser excitation, the NIR-II photoacoustic imaging signal of P-SOH NPs increased in an obvious gradient with the increase in concentration, while W-SOH NPs showed weak photoacoustic signals at the same concentration. The quantitative intensities in Fig. 7b indicated that the photoacoustic intensity of P-SOH NPs was significantly higher than that of W-SOH NPs. The photoacoustic spectrum of P-SOH NPs (Fig. 7c) showed that the peak of the photoacoustic signal was consistent with the absorption peak position (1120 nm), further confirming the formation of the aggregation peak. After tail vein injection of P-SOH NPs, NIR-II photoacoustic imaging of mice could clearly identify heterogeneity of tumor blood vessels (Fig. 7d). The tumor angiography analysis of P-SOH NPs (Fig. 7d) revealed that they could accurately distinguish the microvessels in the tumor area, including capillary branches. The minimum detectable FWHM of blood vessels was only 0.11 mm, and the maximum SBR reached 17.2, indicating an excellent signal contrast between blood vessels and surrounding tissues. Thus, P-SOH NPs were capable of high-resolution tumor angiography.

Evaluation of phototoxicity and biosafety of P-SOH NPs at the *in vivo* level

We further evaluated the phototoxicity and biosafety of P-SOH NPs at the *in vivo* level. As shown in Fig. 8a and b, after tail vein injection of P-SOH NPs, the photoacoustic signal at the tumor site gradually increased over time, reached the peak at 6 h post-injection, and then slowly decreased. This indicated

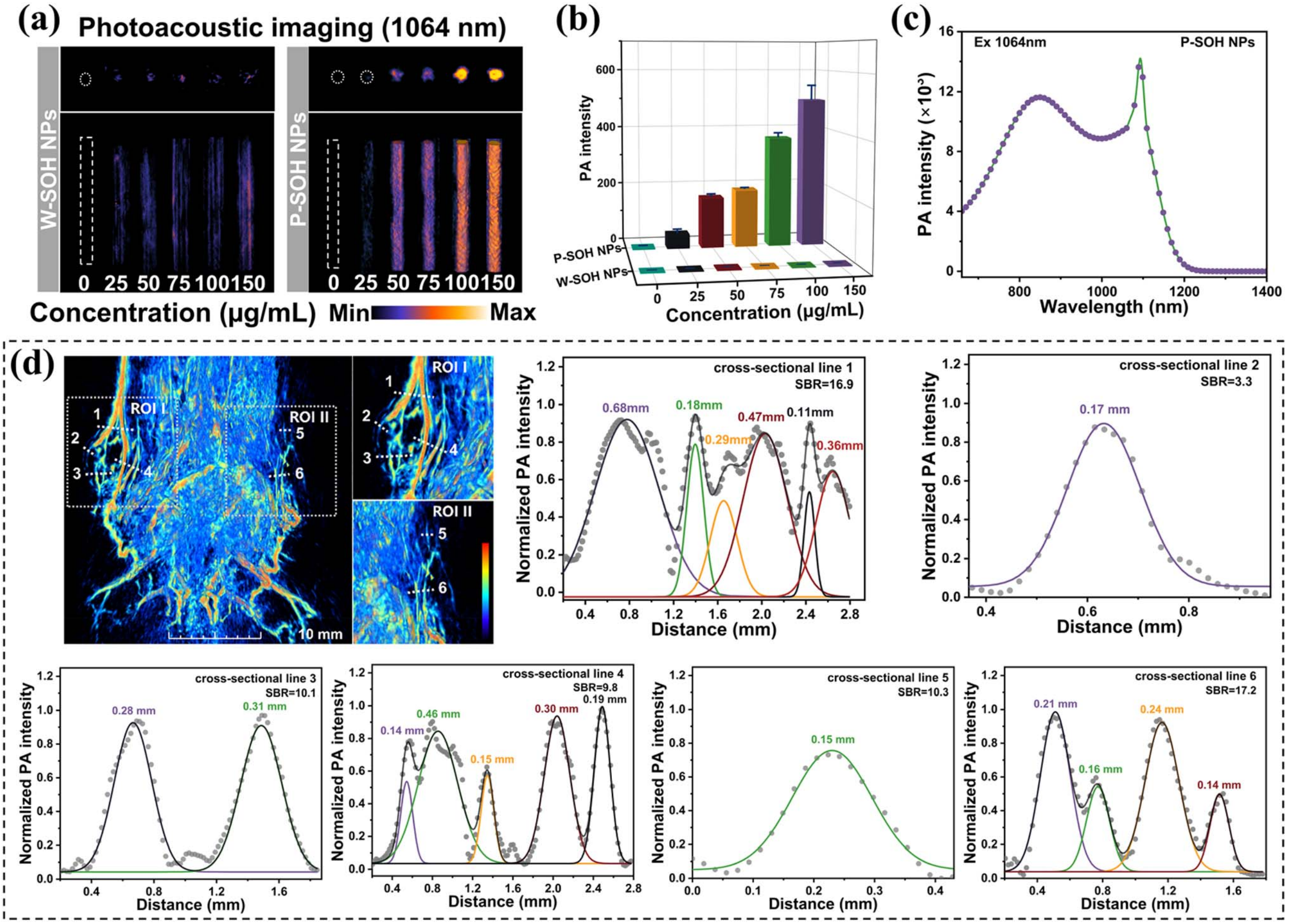

Fig. 7 (a) NIR-II photoacoustic images of W-SOH NPs and P-SOH NPs at different concentrations. (b) Quantification of NIR-II photoacoustic intensities of W-SOH NPs and P-SOH NPs at different concentrations. (c) NIR-II photoacoustic spectrum of P-SOH NPs. (d) NIR-II photoacoustic image and tumor angiography analysis of mice after tail vein injection of P-SOH NPs.

that P-SOH NPs achieved targeted enrichment through the enhanced permeability and retention (EPR) effect of tumors. In contrast, the photoacoustic signal at the tumor site in the W-SOH NP group (Fig. S38a and b) remained weak throughout the observation period. Fig. S39a–e show that P-SOH NPs were mainly distributed in the liver, spleen, and kidneys after injection, suggesting that they were metabolized primarily through hepatobiliary and renal pathways. However, the signals of W-SOH NPs in various organs were relatively weak.

U87-MG subcutaneous tumor-bearing mice were randomly divided into 6 groups for different treatments. As presented in Fig. 8c and d, 6 h after tail vein injection of P-SOH NPs, laser irradiation was performed. The temperature at the tumor site in the P-SOH NPs + L group rapidly increased to 56.3 °C within 10 min. In contrast, the tumor temperature in the W-SOH NPs + L group only increased to 45.4 °C, and there was no significant temperature increase in the PBS + L group (43.3 °C). This result directly verified the efficient photothermal conversion ability of P-SOH NPs *in vivo* (PCE = 51.1%). As shown in Fig. 8e–g, 14 days after treatment, the tumors in the P-SOH NPs + L group were completely ablated, while the tumors in the W-SOH NPs + L group were barely eliminated. Tumors in the PBS, PBS + L, W-SOH NP, and P-SOH NP groups (without laser irradiation) all showed a rapid proliferation trend. The tumor section staining images (Fig. 8i) revealed that the P-SOH NPs + L group showed extensive tumor cell necrosis (cytoplasmic coagulation and nuclear fragmentation) from the hematoxylin and eosin (H & E) staining image, with a low positive rate of Ki-67 (a cell proliferation marker) and a high positive rate of TUNEL (a cell apoptosis marker). In contrast, tumor cells in other groups maintained intact morphology, with a high positive rate of Ki-67 and a low positive rate of TUNEL. These results demonstrated that the phototherapy mediated by P-SOH NPs led to effective elimination of tumors.

During the treatment period, the body weight of mice in all groups remained stable (Fig. 8h). H & E staining images of major organs (Fig. S40) showed that the tissue structure of all organs was intact, with no pathological changes such as inflammatory infiltration or cell necrosis, indicating that P-SOH NPs caused no obvious damage to normal tissues. The hemolysis test (Fig. S41) showed that the hemolysis rates of P-SOH NPs and W-SOH NPs were lower than 3.5% (below the clinical safety threshold of 5%), confirming their good blood compatibility. Blood routine parameters (Fig. S42) and serum

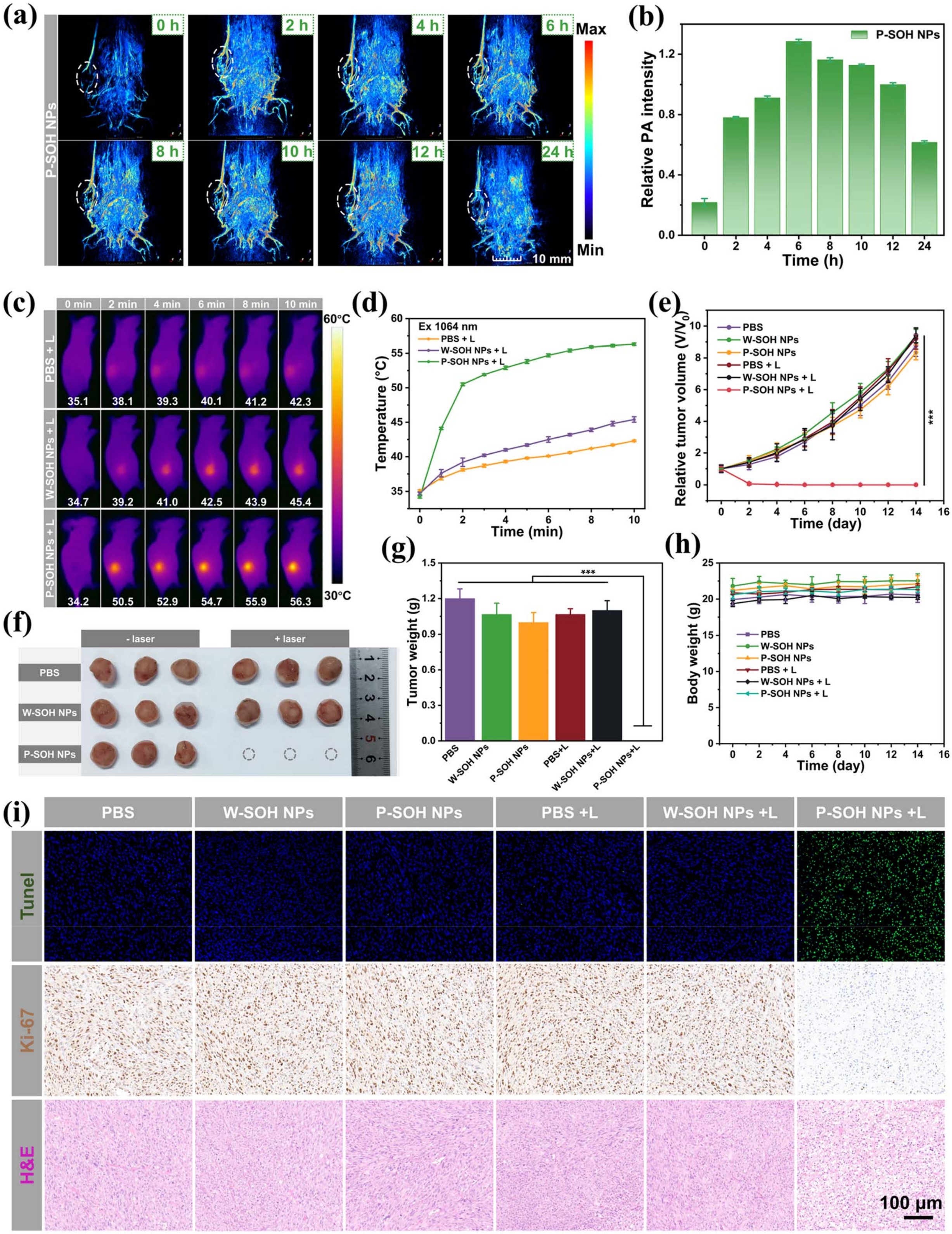

Fig. 8 (a) NIR-II photoacoustic images of mice at different time points after tail vein injection of P-SOH NPs. (b) Quantified photoacoustic intensity at the tumor site. (c) Thermal images of mice after different treatments. (d) Temperature changes at the tumor site of mice after different treatments. (e) Changes in tumor volume of mice in each group during treatment. (f) Images of dissected tumors from mice in each group 14 days after treatment. (g) Weights of dissected tumors from mice in each group. $N = 3$ for each group; ***$p < 0.001$. (h) Changes in body weight of mice in each group during treatment. (i) Hematoxylin and eosin (H & E), Ki-67, and TUNEL staining images of tumor sections from mice in each group after different treatments.

biochemical indicators (Fig. S43) showed that after injection of P-SOH NPs, the blood routine parameters and liver and kidney function indicators of mice were all within the normal physiological range, with no significant difference from the healthy control group. This further confirmed that P-SOH NPs had no adverse effects on the blood system, liver, or kidney function.

Conclusion

Through precise sulfur atom engineering and innovative aggregate regulation strategies, we successfully developed a novel NIR-II thioxanthene dye SOH and its CT-coupled *J*-aggregates, which integrate bimodal NIR-II tumor angiography and efficient phototherapy for hypoxic tumors. The introduction of sulfur atoms was the core innovation for optimizing the photophysical and photochemical properties of the dye. Its strong electron-donating ability promoted ICT, realizing a redshift of absorption/emission spectra and enhancement of the molar extinction coefficient. The heavy atom effect and higher twisted conjugated skeleton strengthened SOC by 9.3-fold, increasing the ISC efficiency by 86.5-fold and elevating PCE to 42.3%. Meanwhile, it reduced the T_1 energy level to 0.959 eV, fundamentally inhibiting the generation of $^1O_2$ and specifically initiating the electron transfer pathway to generate $O_2^{\bullet-}$ and $^{\bullet}OH$. Phosphate-driven aggregate engineering further amplified the therapeutic potential: the specific electrostatic interactions between HPO_4^{2-} and the positively charged regions on the SOH molecular surface induced the formation of CT-coupled *J*-aggregates (P-SOH NPs), synergistically enhancing the NIR-II fluorescence intensity (36.1-fold), type I ROS generation capacity (59.0-fold), and PCE (51.1%), thus overcoming the challenge that it is difficult for a single molecular design to balance multiple performances. P-SOH NPs achieved bimodal high-resolution NIR-II fluorescence/photoacoustic tumor angiography and oxygen-independent synergistic therapy. NIR-II fluorescence imaging could clearly identify tumor microvessels (resolution: 0.34 mm; SBR = 4.56), and NIR-II photoacoustic imaging could accurately delineate the vascular network (resolution: 0.11 mm; SBR = 17.2), providing double guarantees for precise tumor localization. The synergistic effect of type I PDT and PTT maintained a high tumor cell killing efficiency even in hypoxic environments, achieving complete ablation of tumors in tumor-bearing mice with excellent biocompatibility and no obvious organ damage or hematotoxicity.

Ethical statement

All animal procedures were performed in accordance with the Guidelines for Care and Use of Laboratory Animals of Linyi University and approved by the Animal Ethics Committee of Linyi University (approval number: LYU20240803).

Author contributions

Chuangli Zhang: conceptualization, methodology, data curation, investigation, validation, formal analysis, supervision, funding acquisition, visualization, resources, writing – original draft, writing – review and editing, project administration, software. Ziyong Wu: methodology, software, data curation, investigation, formal analysis. Yang Bai, Jing He, Mengyuan Miao, Feiyu Diao, Qingzhi Wang and Shan Zhong: data curation, formal analysis, software. Pengfei Shi: supervision, project administration, resources, funding acquisition. Xinyue Song: supervision. Shusheng Zhang: supervision, funding acquisition, resources.

Conflicts of interest

The authors declare no competing financial interest.

Data availability

The data that support the findings of this study are available from the corresponding author upon reasonable request. Supplementary information (SI): experimental procedures, characterization data, and supporting figures and tables. See DOI: https://doi.org/10.1039/d6sc01958g.

Acknowledgements

This work was supported by the National Natural Science Foundation of China (Grant No. 62305143, 22274068, and 22576090), Natural Science Foundation of Shandong Province (No. ZR2023QB148), Shandong Province Higher Education Institution Youth Innovation Team Project (No. 2024KJG082), Major Basic Research Project of Natural Science Foundation of Shandong Province (No. ZR2023ZD27), Key R&D Program of Shandong Province (2025CXPT112), and Key Project of the Open Research Program of the National Center for Translational Medicine (Shanghai) (TMSK-2024-305 and TMSK-2024-307).

References

1 Z. Chen, F. F. Han, Y. Du, H. Q. Shi and W. C. Zhou, *Signal Transduction Targeted Ther.*, 2023, **8**, 1047–1069.
2 Y. L. Wan, L. H. Fu, C. Y. Li, J. Lin and P. Huang, *Adv. Mater.*, 2021, **33**, 2103978.
3 Y. Jiang, S. M. Huang, H. Y. Ma, J. T. Weng, X. M. Du, Z. X. Lin, J. W. Kim, W. H. You, H. T. Zhang, D. Q. Wang, J. S. Kim and H. Y. Sun, *J. Am. Chem. Soc.*, 2024, **146**, 25270–25281.
4 G. X. Feng, G. Q. Zhang and D. Ding, *Chem. Soc. Rev.*, 2020, **49**, 8179–8234.
5 E. Pang, S. J. Zhao, B. H. Wang, G. L. Niu, X. Z. Song and M. H. Lan, *Coord. Chem. Rev.*, 2022, **472**, 214780.
6 J. H. Zhuang, G. B. Qi, Y. C. Feng, M. Wu, H. Zhang, D. D. Wang, X. H. Zhang, K. C. Chong, B. W. Li, S. T. Liu, J. W. Tian, Y. Shan, D. Mao and B. Liu, *Nat. Commun.*, 2024, **15**, 4943.
7 N. Mohanto, H. Mondal, Y. J. Park and J. P. Jee, *J. Nanobiotechnol.*, 2025, **23**, 25.

8 Y. C. Chen, Y. J. Liu, C. L. Lee, K. Y. Pham, D. Manoharan, S. Thangudu, C. H. Su and C. S. Yeh, *Adv. Healthcare Mater.*, 2022, **11**, 2201613.

9 Q. Ren, Y. Y. Sheng, C. Tao, S. N. Niu, N. Yu, Z. G. Chen and W. S. Lian, *J. Colloid Interface Sci.*, 2024, **668**, 88–97.

10 M. L. Li, J. H. Xiong, Y. Y. Zhang, Y. Lu, L. Z. Yue, C. Yoon, Y. Kim, Y. Zhou, X. Q. Chen, Y. J. Xu, X. J. Peng and J. S. Kim, *Chem. Soc. Rev.*, 2025, **54**, 7025–7057.

11 K. X. Teng, L. Y. Niu, J. H. Li, D. S. Zhang and Q. Z. Yang, *Angew. Chem., Int. Ed.*, 2025, **64**, e202509416.

12 M. X. Jia, Y. H. Pan and W. B. Hu, *Small Methods*, 2025, **9**, e01279.

13 Y. Y. Zhang, M. Zhao, J. Miao, W. Gu, J. L. Zhu, B. L. Cheng, Q. Li and Q. Q. Miao, *ACS Mater. Lett.*, 2023, **5**, 3058–3067.

14 C. L. Zhang, J. S. Wu, W. M. Liu, W. J. Zhang, C. S. Lee and P. F. Wang, *Small*, 2022, **18**, 2202078.

15 H. Wang, K. F. Xue, Y. C. Yang, H. Hu, J. F. Xu and X. Zhang, *J. Am. Chem. Soc.*, 2022, **144**, 2360–2367.

16 S. J. Zhen, Z. Xu, M. Suo, T. Zhang, M. Lyu, T. W. Li, T. F. Zhang, M. J. Li, Z. J. Zhao and B. Z. Tang, *Adv. Mater.*, 2025, **37**, 2411133.

17 Z. Y. Zhang, Y. Du, X. J. Shi, K. Wang, Q. J. Qu, Q. Liang, X. P. Ma, K. S. He, C. W. Chi, J. Q. Tang, B. Liu, J. F. Ji, J. Wang, J. H. Dong, Z. H. Hu and J. Tian, *Nat. Rev. Clin. Oncol.*, 2024, **21**, 449–467.

18 F. F. Wang, Y. T. Zhong, O. Bruns, Y. Y. Liang and H. J. Dai, *Nat. Photonics*, 2024, **18**, 535–547.

19 E. L. Schmidt, Z. H. Ou, E. Ximendes, H. Cui, C. H. C. Keck, D. Jaque and G. S. Hong, *Nat. Rev. Methods Primers*, 2024, **4**, 23.

20 C. L. Zhang, J. S. An, J. S. Wu, W. M. Liu, H. Rha, J. S. Kim and P. F. Wang, *Biosens. Bioelectron.*, 2022, **217**, 114701.

21 Y. X. Ren, X. Y. Zhang, L. Li, Q. Yuan, B. K. Bao, M. Q. Li and Y. L. Tang, *Chem. Sci.*, 2025, **16**, 5089.

22 Q. Wang, J. W. Liu, L. Q. Yang, Z. Tao, J. F. Feng, S. Li, X. Y. Wang, L. Gao, W. H. Tang and Q. L. Fan, *Adv. Funct. Mater.*, 2025, **35**, 2423165.

23 Z. R. Xu, X. Li, Z. M. Yang, Z. J. Zhang, Y. B. Zhang, M. Z. Fan, Y. Y. Zeng, M. M. Kang, Y. Y. Shen, D. Wang, G. X. Xu and B. Z. Tang, *Adv. Mater.*, 2025, **37**, 2413164.

24 H. Chen, Y. Wang, Z. X. He, Y. P. Wan, C. Cao, Z. W. Lu, Y. J. Gao, X. Cui, K. W. Lee, J. H. Tan, W. C. Xu, Y. L. Yang, X. L. Li, Y. L. Wang, J. Q. Hou, S. L. Li and C. S. Lee, *Adv. Mater.*, 2025, **37**, 2501919.

25 C. B. Xiang, Q. H. Ding, T. Jiang, Y. Liu, C. Li, X. Yang, J. Jia, J. J. Xiang, Y. Wang, H. Zhou, Z. Y. Lu, P. Gong and J. S. Kim, *Biomaterials*, 2025, **320**, 123235.

26 T. Shao, L. Han, Y. Xie, Z. X. Shi, Q. L. Yang, A. J. Liu, Y. Liu, L. L. Chen, J. M. Huang, B. Peng, H. Bai, H. L. Chen, L. Li and K. Bian, *Small*, 2025, **21**, 2412249.

27 H. C. Xiao, Y. R. Wang, J. Chen, S. M. Xi, Z. Y. Duan, Q. Y. Zhan, Y. Tian, L. Wang, J. Q. Qu and R. Y. Liu, *Adv. Healthcare Mater.*, 2024, **13**, 2303183.

28 L. Q. Li, C. Shao, T. Liu, Z. C. Chao, H. L. Chen, F. Xiao, H. M. He, Z. X. Wei, Y. Zhu, H. Wang, X. D. Zhang, Y. T. Wen, B. Yang, F. He and L. L. Tian, *Adv. Mater.*, 2020, **32**, 2003471.

29 B. Wang, H. Zhou, L. Chen, Y. C. Ding, X. Y. Zhang, H. Y. Chen, H. Y. Liu, P. Li, Y. Chen, C. Yin and Q. L. Fan, *Angew. Chem., Int. Ed.*, 2024, **63**, e202408874.

30 H. J. Ma, Y. B. An, Y. Y. Han, F. F. Zhao, Y. F. Zuo, G. K. He, Z. X. Lu, R. T. K. Kwok, J. W. Sun, J. W. Y. Lam, Y. Wei and B. Z. Tang, *Adv. Sci.*, 2025, **12**, e07956.

31 J. H. Zhang, J. J. Shao, W. L. Wang, L. C. Wang, X. H. Ruan, K. Xu, P. Chen, X. C. Dong and J. Q. Chen, *Chem. Eng. J.*, 2025, **520**, 166335.

32 X. M. Hu, Z. T. Fang, F. W. Sun, C. J. Zhu, M. X. Jia, X. F. Miao, L. T. Huang, W. B. Hu, Q. L. Fan, Z. Yang and W. Huang, *Angew. Chem., Int. Ed.*, 2024, **63**, e202401036.

33 H. Li, Y. Gu, Y. F. Ding, J. Huang, Z. Q. Yang, P. B. Ding, M. Y. Wang, L. Han, B. Yang, L. Guo, Y. Z. Zhang, F. He and L. L. Tian, *Angew. Chem., Int. Ed.*, 2025, **64**, e202423023.

34 K. K. Wen, H. Tan, Q. Peng, H. Chen, H. Ma, L. Wang, A. D. Peng, Q. Q. Shi, X. D. Cai and H. Huang, *Adv. Mater.*, 2022, **34**, 2108146.

35 X. Y. Zhang, L. F. Yang, M. X. Jia, R. Z. Chen, H. L. Zhang, S. W. Yao, R. D. Bai, Y. Q. Tian, B. Z. Chen, J. Li and W. B. Hu, *Adv. Mater.*, 2025, **10**, e13693.

36 S. M. Wu, W. Z. Zhang, C. R. Li, Z. G. Ni, W. F. Chen, L. Z. Gai, J. W. Tian, Z. J. Guo and H. Lu, *Chem. Sci.*, 2024, **15**, 5973–5979.

37 T. C. Shi, X. Chen, X. L. Li, X. Li, Y. Zhao, H. Y. Zhang, F. P. Han, L. H. Cai, X. Zhou, Y. Su, W. Sun, J. J. Du, J. L. Fan and X. J. Peng, *ACS Nano*, 2025, **19**, 27845–27859.

38 P. F. Chen, L. L. He, K. Chen, Q. Y. Pan, J. Rong, Q. B. Mei, P. F. Sun, C. Zhang and D. F. Li, *Biomaterials*, 2025, **323**, 123435.

39 D. D. Ma, H. Bian, F. Pan, D. H. Zhou, Z. Chen, H. Y. Ge, Y. L. Guo, Y. N. Wu, X. He, P. W. Zhou, L. Wang, X. Q. Chen and X. J. Peng, *Chem. Sci.*, 2026, **17**, 8061.

40 H. Bian, D. D. Ma, Y. H. Chen, J. Hong, Y. Nan, H. Xu, M. H. Kim, X. Q. Chen, X. J. Peng and J. Yoon, *Chem. Soc. Rev.*, 2026, **55**, 3139.

41 H. Bian, D. D. Ma, X. F. Zhang, K. Xin, Y. J. Yang, X. J. Peng and Y. Xiao, *Small*, 2021, **17**, 2100398.

42 A. L. Spearman, E. Y. Lin, E. B. Mobley, A. Chmyrov, B. A. Arús, D. W. Turner, C. A. Garcia, K. Bui, C. Rowlands, O. T. Bruns and E. M. Sletten, *J. Am. Chem. Soc.*, 2025, **147**, 17384–17393.

43 R. T. Ge, F. Xiong, Z. B. Chen, Y. J. Wang, L. Zheng, J. Zhou, D. Wu and S. Y. Zhang, *Chem*, 2025, **11**, 102489.

44 Y. P. Wan, W. L. Chen, Y. Liu, K. W. Lee, Y. J. Gao, D. Zhang, Y. Q. Li, Z. M. Huang, J. D. Luo, C. S. Lee and S. L. Li, *Adv. Mater.*, 2024, **36**, 202405966.

45 X. J. Shi, Z. Zhang, Z. Y. Zhang, C. G. Cao, Z. Cheng, Z. H. Hu, J. Tian and N. Ji, *IEEE Trans. Biomed. Eng.*, 2022, **69**, 1889–1900.

46 C. G. Cao, Z. P. Jin, X. J. Shi, Z. Zhang, A. Q. Xiao, J. Y. Yang, N. Ji, J. Tian and Z. H. Hu, *IEEE Trans. Biomed. Eng.*, 2022, **69**, 2404–2413.

47 Y. F. Ou, H. Y. Xiang, X. Yang, R. X. Wang, S. Y. Huan, L. Yuan, T. B. Ren and X. B. Zhang, *Angew. Chem., Int. Ed.*, 2025, **64**, e202423978.

48 X. Y. Ran, P. Chen, Y. Z. Liu, L. Shi, X. Chen, Y. H. Liu, H. Zhang, L. N. Zhang, K. Li and X. Q. Yu, *Adv. Mater.*, 2023, **35**, 2210179.

49 Q. C. Lan, P. Yu, K. Yan, X. M. Li, F. Zhang and Z. H. Lei, *J. Am. Chem. Soc.*, 2022, **144**, 21010–21015.

50 Z. Y. Wu, C. L. Zhang, J. Sha, Z. Y. Jing, J. He, Y. Bai, J. S. Wu, S. S. Zhang and P. F. Shi, *Anal. Chem.*, 2024, **96**, 5134–5142.

51 C. L. Zhang, J. S. Wu, W. M. Liu, W. J. Zhang, C. S. Lee and P. F. Wang, *Acta Biomater.*, 2023, **159**, 247–258.

52 Y. Bai, C. L. Zhang, Z. Y. Wu, J. He, X. Y. Zhao, A. Y. Zhang, P. F. Shi and S. S. Zhang, *Anal. Chem.*, 2025, **97**, 24833–24848.

53 J. He, Z. Y. Wu, C. L. Zhang, Y. Bai, X. T. Qi, P. F. Shi and S. S. Zhang, *Sens. Actuators, B*, 2026, **449**, 139150.

54 X. Wang, X. W. Han, X. Y. Tian, H. Lee, C. H. Xiang, C. R. Wang, L. Luo, H. Y. Hu, G. L. Niu and J. Yoon, *J. Am. Chem. Soc.*, 2025, **147**, 27068–27080.

55 H. Bian, D. D. Ma, X. D. Zhang, Y. T. Qiu, X. Wu, M. Y. Jia, X. F. Zhang, X. G. Liu, Y. J. Yang, X. J. Peng, J. Yoon and Y. Xiao, *J. Am. Chem. Soc.*, 2025, **147**, 39936–39952.

56 D. Y. Yan, Z. J. Zhang, J. Y. Zhang, X. Li, Q. Wu, Y. X. Gui, J. Zhu, M. M. Kang, X. H. Chen, B. Z. Tang and D. Wang, *Angew. Chem., Int. Ed.*, 2024, **63**, e202401877.

57 D. M. Zhou, G. Q. Zhang, J. Y. Li, Z. Y. Zhuang, P. C. Shen, X. Y. Fu, L. R. Wang, J. Qian, A. J. Qin and B. Z. Tang, *ACS Nano*, 2024, **18**, 25144–25154.

58 T. Xiong, Y. C. Chen, Q. Peng, X. Zhou, M. L. Li, S. Lu, X. Q. Chen, J. L. Fan, L. Wang and X. J. Peng, *Adv. Mater.*, 2025, **37**, 2410992.

59 S. K. Yao, F. W. Xu, Y. Wang, J. Z. Shang, S. M. Li, X. Y. Xu, Z. P. Liu, W. J. He, Z. J. Guo and Y. C. Chen, *J. Am. Chem. Soc.*, 2025, **147**, 11132–11144.

60 B. L. Lu, L. Y. Wang, H. Tang and D. R. Cao, *J. Mater. Chem. B*, 2023, **11**, 4600–4618.